

Tabor Clay, R (Orcid ID: 0000-0002-9915-6157)
Otto-Bliesner Bette, L (Orcid ID: 0000-0003-1911-1598)
Brady Esther, C. (Orcid ID: 0000-0001-7833-2249)
Nusbaumer Jesse (Orcid ID: 0000-0002-4370-3537)
Erb Michael (Orcid ID: 0000-0002-1187-952X)
Wong Tony, E (Orcid ID: 0000-0002-7304-3883)
Noone David (Orcid ID: 0000-0002-8642-7843)

Interpreting precession driven $\delta^{18}\text{O}$ variability in the South Asian monsoon region

Clay R. Tabor¹, Bette L. Otto-Bliesner², Esther C. Brady², Jesse Nusbaumer³, Jiang Zhu⁴, Michael P. Erb⁵, Tony E Wong⁶, Zhengyu Liu⁷, David Noone⁸

¹ Center for Integrative Geosciences, University of Connecticut, Storrs, CT

² Climate & Global Dynamics Lab, National Center for Atmospheric Research, Boulder, CO

³ NASA Goddard Institute for Space Studies, New York, NY

⁴ Department of Earth and Environmental Sciences, University of Michigan, Ann Arbor, MI

⁵ Earth Sciences and Environmental Sustainability, Northern Arizona University, Flagstaff, AZ

⁶ Department of Computer Science, University of Colorado Boulder, Boulder, CO

⁷ Atmospheric Science Program, Department of Geography, Ohio State University, Columbus, OH

⁸ College of Earth, Ocean, and Atmospheric Sciences, Oregon State University, Corvallis, OR

Corresponding author: Clay Tabor (clay.tabor@uconn.edu)

This is the author manuscript accepted for publication and has undergone full peer review but has not been through the copyediting, typesetting, pagination and proofreading process, which may lead to differences between this version and the [Version of Record](#). Please cite this article as doi: [10.1029/2018JD028424](https://doi.org/10.1029/2018JD028424)

Key Points:

- Used an Earth system model with stable water isotope tracers to examine precession driven variability of the South Asian Monsoon
- South Asian Monsoon variability in $\delta^{18}\text{O}$ of precipitation is due to changes in the amount of moisture sourced from different regions
- Using simulated $\delta^{18}\text{O}$ of soil water improves model-speleothem signal agreement

Abstract

Speleothem records from the South Asian summer monsoon (SASM) region display variability in the ratio of ^{18}O and ^{16}O ($\delta^{18}\text{O}$) in calcium carbonate at orbital frequencies. The dominant mode of variability in many of these records reflects cycles of precession. There are several potential explanations for why SASM speleothem records show a strong precession signal, including changes in temperature, precipitation, and circulation. Here, we use an Earth system model with water isotope tracers and water tagging capability to deconstruct the precession signal found in SASM speleothem records. Our results show that cycles of precession-eccentricity produce changes in SASM intensity that correlate with local temperature, precipitation, and $\delta^{18}\text{O}$. However, neither the amount effect nor temperature differences are responsible for the majority of the SASM $\delta^{18}\text{O}$ variability. Instead, changes in the relative moisture contributions from different source regions drive much of the SASM $\delta^{18}\text{O}$ signal, with more nearby moisture sources during Northern Hemisphere summer at aphelion and more distant moisture sources during Northern Hemisphere summer at perihelion. Further, we find that evaporation amplifies the $\delta^{18}\text{O}$ signal of soil water relative to that of precipitation, providing a better match with the SASM speleothem records. This work helps explain a significant portion of the long-term variability found in SASM speleothem records.

1 Introduction

Today, millions of people depend on the seasonal rains associated with the SASM.

During the summer months, a reversal of upper tropospheric temperatures between India and the equator marks the onset of the SASM rainy season (e.g., He et al, 1987; Webster and Yang, 1992; Webster et al., 1998). Establishment of an off-equator meridional overturning circulation moves deep convection over the Indian subcontinent, resulting in a seasonal precipitation anomaly (e.g., Plumb and Hou, 1992; Prive and Plumb, 2007a,b; Feng et al., 2011). The typical SASM wet season lasts from June to October and accounts for the majority of annual precipitation over India (e.g., Fasullo and Webster, 2003).

While SASM evolution is well observed, debate continues about the mechanisms driving its formation and variability (Molnar et al., 2010). The traditional view states that a large influx of sensible heat from the surface of the Tibetan Plateau to the middle troposphere results in local ascent; plateau heating draws low-level moist air northward, which promotes convergence and latent heat release, driving the SASM circulation (e.g., Li and Yanai, 1996; Yanai and Wu, 2006). However, recent observations and modeling work question this traditional explanation (Boos, 2015). An alternative hypothesis, supported by climate model simulations, proposes that the Himalayas and Tibetan Plateau act as a barrier between cold, dry extratropical air to the north and warm, moist tropical air to the south (e.g., Chakraborty et al., 2006; Boos and Kuang, 2010). Here, direct heating produces the meridional gradients while the land barriers maintain the moist static energy maximum that develops in Northern India. In this view, sensible heating from the Tibetan Plateau is not directly linked to the SASM circulation. Finally, another recent theory suggests that direct and indirect heating from Himalayas and adjacent mountain ranges plays an

important role in the strength and circulation of the SASM (Wu et al., 2012; Chen et al., 2014).

Understanding the mechanisms driving the formation and variability of SASM can benefit from studying the past. Under present-day conditions, the strength of the SASM is fairly consistent from year to year, with summer precipitation fluctuations of only ~20% between the strongest and weakest monsoons (e.g., Gadgil, 2003). However, cave records from Northern India hint at significant multi-millennial scale variability of the SASM during the late Quaternary (Cai et al., 2010; 2015; Kathayat et al., 2016). These cave records, known as speleothems, chronicle $\delta^{18}\text{O}$ of dripwater in calcium carbonate ($\delta^{18}\text{O}_c$) via CaCO_3 precipitation (McDermott, 2004). In combination with precise age control from U-series dating, speleothem records provide some of the best evidence for past hydrological change in the SASM region.

Often, some of the greatest amplitude $\delta^{18}\text{O}_c$ signal in Asian speleothems exists at the 23- kyr^{-1} frequency of precession (e.g., Cheng et al, 2012; Cai et al., 2006; Cai et al., 2015; Kathayat et al., 2016). Many attribute this $\delta^{18}\text{O}_c$ cyclicity to changes in the Asian monsoon, with greater monsoon intensity corresponding to more negative $\delta^{18}\text{O}_c$. Climate model simulations agree that precession, together with eccentricity modulation, drives changes in SASM intensity (e.g., Kutzbach and Otto-Bliesner, 1982; Liu et al., 2006; Kutzbach et al., 2008; Battisti et al., 2014; Bosman et al., 2018). During precession-eccentricity induced periods of anomalously high Northern Hemisphere summer insolation, the SASM summer precipitation is more intense, and vice versa. This positive correlation between Northern Hemisphere summer insolation and precipitation intensity of the SASM supports the theory that insolation is more or less a direct

driver of monsoon intensity (e.g., Kutzbach, 1981; Kutzbach and Otto-Bliesner, 1982; Ruddiman, 2006). Nevertheless, records from the Arabian Sea lag maximum Northern Hemisphere summer insolation by roughly 8 kyr, which, if driven by the same mechanisms, contradicts the direct forcing Asian monsoon interpretation of climate models and Asian speleothem records (Clemens and Prell, 1991; Clemens and Prell, 2007; Clemens et al., 2010).

The mechanisms responsible for precipitation-weighted $\delta^{18}\text{O}$ ($\delta^{18}\text{O}_{\text{wp}}$) variability in the SASM region with changes in precession-eccentricity are difficult to decipher. Variability in SASM $\delta^{18}\text{O}_{\text{wp}}$ is not necessarily a product of changes in precipitation intensity (e.g., Battisti et al., 2014), known as the “amount effect” (Dansgaard, 1964). The $\delta^{18}\text{O}_{\text{wp}}$ signal in the SASM region can also be altered by changes in $\delta^{18}\text{O}$ of water vapor ($\delta^{18}\text{O}_{\text{wv}}$) from moisture sources, the relative amount of precipitation from moisture sources, rainout of water vapor during transport, and seasonality of precipitation (e.g., Pausata et al., 2011, Caley et al., 2014). Potential disconnects between $\delta^{18}\text{O}_{\text{wp}}$ and $\delta^{18}\text{O}_{\text{c}}$ in the speleothem records, such as mixing of water sources and soil and karst processes, compound the complexity (e.g., Fairchild et al. 2006; Baker et al., 2012). Further, changes in cave temperature at the time of calcium carbonate deposition can alter the $\delta^{18}\text{O}_{\text{c}}$ value (Friedman and O’Neil, 1977). Before we can attribute $\delta^{18}\text{O}_{\text{c}}$ variability in speleothems to past hydrological changes, we must disentangle these confounding influences.

Isotope-enabled Earth system models provide a novel approach for understanding variability in speleothem $\delta^{18}\text{O}_{\text{c}}$ records. By tracking the physical and dynamical movement of H_2^{18}O and H_2^{16}O within the earth system, we can better determine what mechanisms are

responsible for the $\delta^{18}\text{O}_c$ signals found in the SASM speleothems. Indeed, previous climate simulations with water isotope tracers have helped us understand the mechanisms responsible for $\delta^{18}\text{O}_{wp}$ changes in the SASM region due to Heinrich events (Pausata et al., 2011), topographic and land-ice changes (Caley et al., 2014; Roe et al., 2016), long-term orbital variability (Battisti et al., 2014; Liu et al., 2014; Caley et al., 2014), and present-day annual fluctuations (Vuille et al., 2005), as well as $\delta^{18}\text{O}_{wp}$ changes across other topographically complex regions and geological time periods (e.g., Poulsen et al., 2010; Feng et al., 2013; 2016).

Here, we use a fully coupled, state-of-the-art Earth system model with water isotope tracking capability to explore the SASM $\delta^{18}\text{O}$ responses under different configurations of precession-eccentricity. Our simulated $\delta^{18}\text{O}_{wp}$ and $\delta^{18}\text{O}$ soil water ($\delta^{18}\text{O}_{ws}$) changes reflect the $\delta^{18}\text{O}_c$ values found in the SASM speleothem records. Despite the strong relationship between precipitation and $\delta^{18}\text{O}_{wp}$ over India, we find the SASM $\delta^{18}\text{O}_{wp}$ variability is not directly due to the “amount effect”. Instead, we show that changes in the relative contributions from different water vapor sources to the SASM region are mostly responsible for $\delta^{18}\text{O}_{wp}$ variability due to precession-eccentricity. Further, we find that the modeled $\delta^{18}\text{O}_{ws}$ amplitudes better match the $\delta^{18}\text{O}_c$ signals in the SASM speleothems, suggesting that local evaporation may play an important role.

In section 2, we detail the earth system model, experiment configurations, and water tracking techniques that we use to elucidate mechanisms responsible for precession control on $\delta^{18}\text{O}$ variability in the SASM. Then, we present our results, including climatologies over the

Indian subcontinent, changes in dynamics between Northern Hemisphere summers at aphelion and perihelion, and comparison with speleothem records from the SASM region, in section 3. Finally, we summarize our findings in section 4.

2 Methods

2.1 Model

We use a stable water isotope tracer-enabled version of the Community Earth System Model (iCESM1.2), maintained by the National Center for Atmospheric Research (NCAR). Our configuration of iCESM1.2 includes dynamically coupled atmosphere (CAM5), ocean (POP2), land (CLM4), sea ice (CICE4), and river runoff (RTM) components. The atmosphere and land are on a 1.9° latitude x 2.5° longitude finite-volume grid with 30 and 10 vertical levels, respectively. More specifically, CLM4 has 10 hydrologically active soil levels that reach a depth of 3.8 m (Oleson et al., 2010). Soil composition in CLM4 comes from the Geosphere-Biosphere Programme soil dataset (Bonan et al., 2002b; Lawrence and Slater, 2008). The ocean and sea ice use a $\sim 1^\circ$ rotated pole grid. The ocean has 60 vertical levels. This version of CESM well simulates preindustrial and present-day climate (Hurrell et al., 2013). Further, CESM successfully captures the seasonal patterns of SASM precipitation (Meehl et al., 2013), with skill similar to CCSM4 (Meehl et al., 2012c; Sperber et al., 2012). Analyses show that CESM produces one of the best simulations of the SASM among CMIP5 models (Ashfaq et al., 2016).

The stable water isotope tracer-enabled version of iCESM1.2 includes water isotopes of oxygen and hydrogen in all the dynamically coupled model components. Studies show that

iCESM1.2 compares favorably with other isotope-enabled Earth system models of similar complexity (Nusbaumer et al., 2017; Wong et al., 2017). Likewise, a preindustrial iCESM simulation shows generally good agreement with observed spatial patterns of $\delta^{18}\text{O}_p$ and precipitation in and around the SASM region (Figure S1; S2). We direct the reader to the following studies for additional details about the strengths and weaknesses of the water isotope-enabled components: atmosphere (Nusbaumer et al., 2017), land (Wong et al., 2017), ocean (Zhang et al., 2017), and coupled system (Zhu et al., 2017). For this study, we focus on oxygen isotopic responses.

2.2 Simulations

We simulate climate responses to four combinations of precession-eccentricity. To get a maximum precession signal, the eccentricity value in these four simulations is set to 0.0493, which represents the largest value of the past 900 ka (Berger, 1991). The four angles of precession include: Northern Hemisphere perihelion at autumnal equinox (AEQ), winter solstice (WSOL), vernal equinox (VEQ), and summer solstice (SSOL). A fifth experiment with 0 eccentricity (0_ECC) negates the influence of precession angle and serves as a control. Aside from the orbital configurations, we initialize all simulations with the CESM default preindustrial configuration, including greenhouse gas concentrations, aerosol forcings, and vegetation types. While plant functional types cannot evolve, vegetation phenology responds in these simulations to changes in climate conditions.

We run all simulations for at least 500 years to reach quasi-equilibrium climate states

with top-of-atmosphere radiation imbalances less than 0.15 Wm^{-2} . After the simulations reach near-equilibrium, we add water isotope tracers to the model and run each simulation for an additional 550 years. Initial ocean oxygen isotopic distributions come from the GISS interpolated ocean $\delta^{18}\text{O}$ dataset (LeGrande and Schmidt, 2006). While 550 years are not long enough for the deep-ocean to reach a new equilibrium with respect to water isotopes, the upper ocean, land, and atmosphere are in equilibrium. All of our analyses come from averages of the final 50 years of model simulation.

2.3 Analyses

2.3.1 Orbital Calendar

According to Kepler's second law, cycles of precession-eccentricity result in changes in the duration and timing of the seasons. Therefore, using monthly outputs from the fixed Gregorian calendar means that months in different simulations would represent slightly different parts of the Earth's orbit, complicating interpretation of anomalies (e.g., Jousaume and Braconnot, 1997). Instead, we use daily model output to compute monthly averages based on a fixed-angular calendar, in which each "month" is a 30° angle of Earth's orbit around the sun. An angular calendar removes artificial phase shifts resulting from changes in Earth's rate of orbit around the sun under high eccentricity. As in previous works, we align the angular calendar with the vernal equinox on March 21st (Jousaume and Braconnot, 1997; Pollard and Reusch, 2002).

2.3.2 Linear Reconstructions

In section 3.2, we use linear combinations of our simulated idealized climatologies to

reconstruct long-term variations in the SASM. As in Erb et al. (2015), we reconstruct climate change for past periods with different precession and eccentricity using the following equation:

$$1. \Delta X_{\text{prec-ecc}} = \frac{e}{e_{\text{prec}}} \left[\left(\frac{X_{\text{AEQ}} - X_{\text{VEQ}}}{2} \cos \omega + \frac{X_{\text{WSOL}} - X_{\text{SSOL}}}{2} \sin \omega \right) + \left(\frac{X_{\text{AEQ}} + X_{\text{WSOL}} + X_{\text{VEQ}} + X_{\text{SSOL}}}{4} \right) - X_{0_ECC} \right]$$

Here, X is the variable of interest, with each subscript corresponding to the value under that particular orbital configuration. e_{prec} is the value of eccentricity used in the precession simulations (0.0493). e and ω are eccentricity and longitude of perihelion for the time of interest, respectively.

This method assumes linearity in the response of the SASM climate to forcings from precession-eccentricity. Of course, this assumption is not strictly true. However, previous work has demonstrated that aspects of the SASM tend to respond linearly with changes in insolation (Liu et al., 2003; Braconnot et al., 2008; Roe et al., 2015). This linear reconstruction method allows for visual comparison of the amplitudes and phasing between simulated variables and with $\delta^{18}\text{O}_c$ records.

2.3.3 Water Tagging

To better understand $\delta^{18}\text{O}$ changes, we tag 27 locations between 40°S and 70°N (Figure 1). We track the ^{16}O and ^{18}O of water vapor that evaporates from within each tagged region individually. The water-tagging technique helps decipher the mechanisms responsible for $\delta^{18}\text{O}$ changes in the SASM region over cycles of precession-eccentricity. Here, we define the SASM region as the land area between 10 to 30°N and 70 to 100°E.

By tagging water vapor in various regions, we know the origins, rainout history, and isotopic composition of the water that precipitates over the SASM region for SSOL and WSOL. We can use this information to deconstruct how changes in climate between these two extreme orbits alter $\delta^{18}\text{O}_{\text{wp}}$ in the SASM region. For a tagged source region i , its resulting $\delta^{18}\text{O}_{\text{p}}$ signature over the SASM region ($\delta^{18}\text{O}_{\text{psink } i}$) relates to the $\delta^{18}\text{O}_{\text{wv}}$ from its source through a chain relationship:

$$2. \delta^{18}\text{O}_{\text{psink } i} = (\delta^{18}\text{O}_{\text{psink}} - \delta^{18}\text{O}_{\text{wvsink}})_i + (\delta^{18}\text{O}_{\text{wvsink}} - \delta^{18}\text{O}_{\text{wvsource}})_i + (\delta^{18}\text{O}_{\text{wvsource}})_i$$

In equation 2, $(\delta^{18}\text{O}_{\text{wvsource}})_i$ is the $\delta^{18}\text{O}$ of water vapor originating from tagged region i , $(\delta^{18}\text{O}_{\text{wvsink}} - \delta^{18}\text{O}_{\text{wvsource}})_i$ is the effect of rainout on $\delta^{18}\text{O}$ of water vapor along its transport path from tagged region i to the SASM sink, and $(\delta^{18}\text{O}_{\text{psink}} - \delta^{18}\text{O}_{\text{wvsink}})_i$ is the effect of condensation enrichment in ^{18}O of precipitation at the SASM sink. This chain relationship reflects three stages of the evaporation-precipitation process from a water vapor source i to the SASM sink.

The actual $\delta^{18}\text{O}_{\text{wp}}$ value in the SASM region, however, is also dependent on the amount of precipitation from each tagged region, which can be written as:

$$3. \delta^{18}\text{O}_{\text{wp}} = \sum_{i=1}^N \left(\delta^{18}\text{O}_{\text{psink } i} \times \frac{p_i}{p_{\text{total}}} \right)$$

where i is the i^{th} tagged region, N is the total number of tagged regions (p_{total}), and p_i is the precipitation contributed from the i^{th} tagged region to the SASM region. Therefore, changes in $\delta^{18}\text{O}_{\text{wp}}$ in the SASM region result from changes in both $\delta^{18}\text{O}_{\text{psink } i}$ and $\frac{p_i}{p_{\text{total}}}$, which can be expressed as:

$$4. \Delta(\delta^{18}\text{O}_{\text{wp } i}) = \Delta \left(\delta^{18}\text{O}_{\text{psink } i} \times \frac{p_i}{p_{\text{total}}} \right) =$$

$$\Delta \left[(\delta^{18}\text{O}_{\text{psink}} - \delta^{18}\text{O}_{\text{wv sink}})_i + (\delta^{18}\text{O}_{\text{wv sink}} - \delta^{18}\text{O}_{\text{wv source}})_i + (\delta^{18}\text{O}_{\text{wv source}})_i \right] \times$$

$$\frac{p_i}{p_{\text{total}}} +$$

$$\left[(\delta^{18}\text{O}_{\text{psink}} - \delta^{18}\text{O}_{\text{wv sink}})_i + (\delta^{18}\text{O}_{\text{wv sink}} - \delta^{18}\text{O}_{\text{wv source}})_i + (\delta^{18}\text{O}_{\text{wv source}})_i \right] \times$$

$$\Delta \left(\frac{p_i}{p_{\text{total}}} \right)$$

Using the SSOL and WSOL cases, we can rewrite equation 4 for a tagged region i as:

$$5. \Delta(\delta^{18}\text{O}_{\text{wp } i}) = \Delta \left(\delta^{18}\text{O}_{\text{psink } i} \times \frac{p_i}{p_{\text{total}}} \right) =$$

$$(\delta^{18}\text{O}_{\text{psink } i \text{ SSOL}} - \delta^{18}\text{O}_{\text{psink } i \text{ WSOL}}) \times \left(\frac{p_i}{p_{\text{total}}} \right)_{\text{SSOL}} + \delta^{18}\text{O}_{\text{psink } i \text{ SSOL}} \times \left[\left(\frac{p_i}{p_{\text{total}}} \right)_{\text{SSOL}} - \right.$$

$$\left(\frac{p_i}{p_{\text{total}}} \right)_{\text{WSOL}} \Big]$$

From there, we can further decompose $(\delta^{18}\text{O}_{p_{\text{sink } i \text{ SSOL}}} - \delta^{18}\text{O}_{p_{\text{sink } i \text{ WSOL}}})$ into:

$$6. \Delta\delta^{18}\text{O}_{\text{source } i} = \Delta(\delta^{18}\text{O}_{\text{wv}_{\text{source } i}})_i = (\delta^{18}\text{O}_{\text{wv}_{\text{source } i}})_{\text{SSOL}} - (\delta^{18}\text{O}_{\text{wv}_{\text{source } i}})_{\text{WSOL}} + o[\Delta(\delta^{18}\text{O}_{\text{rainout } i} + \delta^{18}\text{O}_{\text{condense } i})_{\text{source}}]$$

$$7. \Delta\delta^{18}\text{O}_{\text{rainout } i} = \Delta(\delta^{18}\text{O}_{\text{wv}_{\text{sink}}} - \delta^{18}\text{O}_{\text{wv}_{\text{source } i}})_i = (\delta^{18}\text{O}_{\text{wv}_{\text{sink } i}} - \delta^{18}\text{O}_{\text{wv}_{\text{source } i}})_{\text{SSOL}} - (\delta^{18}\text{O}_{\text{wv}_{\text{sink } i}} - \delta^{18}\text{O}_{\text{wv}_{\text{source } i}})_{\text{WSOL}} + o[\Delta(\delta^{18}\text{O}_{\text{condense } i})_{\text{rainout}}]$$

$$8. \Delta\delta^{18}\text{O}_{\text{condense } i} = \Delta(\delta^{18}\text{O}_{p_{\text{sink}}} - \delta^{18}\text{O}_{\text{wv}_{\text{sink}}})_i = (\delta^{18}\text{O}_{p_{\text{sink } i}} - \delta^{18}\text{O}_{\text{wv}_{\text{sink } i}})_{\text{SSOL}} - (\delta^{18}\text{O}_{p_{\text{sink } i}} - \delta^{18}\text{O}_{\text{wv}_{\text{sink } i}})_{\text{WSOL}}$$

where $o[\Delta(\delta^{18}\text{O}_{\text{rainout } i} + \delta^{18}\text{O}_{\text{condense } i})_{\text{source}}]$ and $o[\Delta(\delta^{18}\text{O}_{\text{condense } i})_{\text{rainout}}]$ describe higher-order terms of amplification or attenuation of $\Delta\delta^{18}\text{O}_{\text{source } i}$ and $\Delta\delta^{18}\text{O}_{\text{rainout } i}$ through rainout and condensation and through condensation processes, respectively. For isolating the effects of $\delta^{18}\text{O}_{\text{source } i}$ and $\delta^{18}\text{O}_{\text{rainout } i}$ on $\delta^{18}\text{O}_{\text{wp}}$, we assume that these terms are unimportant. This is a simplification because we accept linearity of the $\delta^{18}\text{O}$ responses, which does not hold for some processes such as fractionation during rainout and the effects of temperature change on

fractionation. However, temperature change is of secondary importance in these simulations because summer surface temperature differences (often used to approximate the fractionation temperatures at the cloud base) are small between orbits. In addition to linear approximations, the above equations are inexact because they assume that the average $\delta^{18}\text{O}_{\text{wv}}$ originating from the source regions is the same as the $\delta^{18}\text{O}_{\text{wv}}$ that is transported to the SASM region. In reality, some of the tagged water vapor never reaches the SASM region. With these assumptions in mind, we can explore the effects of precession-eccentricity cycles on the SASM $\Delta\delta^{18}\text{O}_{\text{wp}}$ signal due to changes in source vapor ($\Delta\delta^{18}\text{O}_{\text{source}}$), rainout during transport ($\Delta\delta^{18}\text{O}_{\text{rainout}}$), condensation over the SASM region ($\Delta\delta^{18}\text{O}_{\text{condense}}$), and relative precipitation contribution ($\Delta\left(\frac{P_i}{P_{\text{total}}}\right)$). We discuss these results in section 3.3 and 3.4.

2.3.4 Site Comparisons

Both Bittoo (30°47'N; 77°47'E) and Tianmen cave (30°55'N; 90°4'E) sites are located on the northern edge of the SASM region (Figure 1 stars). These caves contain long term speleothem records that display $\delta^{18}\text{O}_{\text{c}}$ variability at the frequency of precession (Cai et al., 2010; 2015; Kathayat et al., 2016). In order to understand this $\delta^{18}\text{O}_{\text{c}}$ variability, we compare simulated $\delta^{18}\text{O}_{\text{ws}}$ signals constructed by linearly combining end-member precession-eccentricity simulations with the speleothem records. We also create a more representative $\delta^{18}\text{O}_{\text{c}}$ reconstruction using modeled $\delta^{18}\text{O}_{\text{ws}} - 0.24 \text{‰K}^{-1} \times \text{surface temperature}$, which estimates the fractionation response due to changes in cave temperature during stalagmite formation (Friedman and O'Neil, 1977). Model data come from 2° latitude x 2° longitude boxes

surrounding the speleothem collection sites.

3 Results and Discussion

3.1 Seasonal Climatology

Cycles of precession-eccentricity change the seasonal distribution of insolation, which can lead to variations in both seasonal and annual mean climate (Figure 2a; Tuenter et al., 2005; Tabor et al., 2014; 2015). Here, we focus primarily on summer (June, July, August, September; JJAS) climate, because the majority of the SASM precipitation, which produces the $\delta^{18}\text{O}_{\text{wp}}$ signal, falls during this time (Molnar et al., 2010; Battisti et al., 2014). Despite large differences in insolation forcing between simulations, some general SASM climate characteristics persist (Figure 2). For instance, in all four high-eccentricity simulations, between 70 and 76 % of SASM precipitation falls during JJAS, with peak rainfall in July (Figure 2e; Figure 3). As expected, the precipitation maxima generally align with the SAM index (Figure 2i), as defined by the difference in the meridional winds between 850 and 250 hPa and from 10° – 30°N and 70° – 110°E (Goswami et al., 1998), and local 900 hPa equivalent potential temperature (Figure 2h). Further, SASM surface temperatures peak in the late spring due to strong surface heating in all orbital scenarios (Figure 2g; Figure 4). The subsequent arrival of monsoon rains limits additional surface warming through increased cloud cover and soil moisture. In all simulations, SASM maximum evaporation occurs in the summer and fall, generally coinciding with the period of greatest surface moisture availability (Figure 2d,f; Figure 5). Seasonal phasing of $\delta^{18}\text{O}$ is also similar in the SASM region. For both precipitation and soil water, the most positive SASM $\delta^{18}\text{O}$

signals occur in the spring and the most negative $\delta^{18}\text{O}$ signals occur in the fall (Figure 2b,c; Figure 6; Figure 7).

Despite similarities in SASM seasonal cycles between orbits, changes in the timing of precession result in different amplitudes of SASM variability. Going from WSOL to SSOL, July monsoon strength increases by almost 2.5 times, as defined by the SAM index (Goswami et al., 1998) (Figure 2i). Precipitation amount coincides with increasing SASM intensity, with a 43% increase in summer precipitation rate in SSOL relative to WSOL (Figure 2e; Figure 3). Compared to summer, winter (DJFM) precipitation rates in the SASM region are small. While winter precipitation increases by 96 % from SSOL to WSOL, the small absolute values contribute little to the annual $\delta^{18}\text{O}_{\text{wp}}$ signal in both orbits. However, the opposite pattern exists for SASM surface temperature. While insolation plays a large role in SASM intensity, summer surface temperatures are similar for all simulations (Figure 2g; Figure 4); clouds and latent heat loss keep local summer surface temperature to within 1 K among experiments, despite large differences in insolation, at times in excess of 80 Wm^{-2} (Figure 2a). Conversely, all other months show a strong correlation between SASM surface temperature and insolation, relating to more direct surface shortwave heating under dry atmospheric conditions. As an annual mean, SASM surface temperatures reflect dry season insolation. There are also annual mean changes in $\delta^{18}\text{O}_{\text{wp}}$ and $\delta^{18}\text{O}_{\text{ws}}$ (Figure 6; Figure 7). In general, the $\delta^{18}\text{O}_{\text{wp}}$ signals become more depleted with increasing summer insolation intensity. As an annual average, WSOL shows a 1.7 ‰ more positive $\delta^{18}\text{O}_{\text{wp}}$ signal and a 1.9 ‰ more positive $\delta^{18}\text{O}_{\text{ws}}$ signal relative to SSOL in the SASM

region. We discuss the mechanisms responsible for these oxygen isotopic differences in section 3.3.

3.2 Linear Reconstructions

To directly compare with available speleothem $\delta^{18}\text{O}$ records and better understand long-term climate variability in the SASM region, we reconstruct the climatological history due to changes in precession-eccentricity by assuming that linear combinations of the end-member forcings can well replicate the intermediate responses (see methods for details). Here, we reconstruct precession-eccentricity driven SASM variations in annual average surface temperature, precipitation, $\delta^{18}\text{O}_{\text{wp}}$, and $\delta^{18}\text{O}_{\text{ws}}$ over the past 250 ka using equation 1 with calculated orbital parameters (Figure 8; Berger, 1991). While circulation shifts within the SASM region are mechanistically a result of the same phenomenon, the precipitation response is heterogeneous, with the greatest difference between orbits occurring at the southern edge of the Himalayan Mountain range (Figure 3). Consequently, our precipitation and isotopic analyses of the SASM region are weighted towards this area. For contrast, we compare our model results with speleothem records from two specific cave sites in Section 3.6.

For all reconstructed time series, the local maxima and minima roughly coincide with WSOL or SSOL, although small differences in timing do exist. For example, changes in SASM surface temperature, precipitation, and $\delta^{18}\text{O}$ lag precession-driven June insolation by roughly 1 kyr (Figure 8). Simulations with a different model have shown that maximum Northern Hemisphere monsoonal precipitation may not correspond exactly to a SSOL orbital setup (see

Figure 3 in Erb et al. 2015). Further, somewhat greater lags of a few thousand years between summer insolation maxima and $\delta^{18}\text{O}_c$ have been found in many Asian speleothem records (e.g. Wang et al., 2008; Cheng et al., 2016).

Our simulations generally support a summer insolation driver of SASM strength, with a small lag in the monsoon response to peak insolation (Figure 2i; Figure 8). As discussed in Battisti et al. (2014), insolation induced changes in the location of sub-cloud moist entropy produces the SASM circulation. In SSOL, strong insolation leads to a more rapid onset, further northward shift, and larger latitudinal gradient in the moist entropy, which creates a stronger monsoon circulation. This finding is seemingly at odds with Arabian Sea records that have been interpreted as evidence for an 8 kyr offset between summer insolation maxima and peak Asian monsoon intensity (Clemens and Prell, 2006; Clemens et al., 2010). However, our simulations also highlight the complexity of the SASM response to precession-eccentricity forcing (Figure 3-7). We suspect that the Arabian Sea records are capturing other aspects of the monsoon response to orbital cycles (Ruddiman, 2006; Ziegler et al., 2010; Le Mezo et al. 2017). That said, our study is limited to the equilibrium SASM responses of precession-eccentricity forcing. Phasing uncertainties related to influences of other long-term climate drivers, transient Earth system responses, and use of linear interpolation limit our ability to resolve this conundrum.

As alluded to above, the largest July SASM precipitation rate is 13.6 mm/day during SSOL, an increase of 51% from the lowest July SASM precipitation rate of 9.0 mm/day during WSOL. The SASM precipitation signal has a negative relationship with both local $\delta^{18}\text{O}_{wp}$ and

$\delta^{18}\text{O}_{\text{ws}}$ signals (Figure 8a); greatest SASM $\delta^{18}\text{O}_{\text{wp}}$ increase occurs during precipitation minima. Conversely, surface temperature shows a positive relationship with local $\delta^{18}\text{O}_{\text{wp}}$ and $\delta^{18}\text{O}_{\text{ws}}$ due to the strong surface temperature response to dry season insolation (Figure 8b). In our model-based SASM reconstructions, the $\delta^{18}\text{O}_{\text{ws}}$ signal has a greater maximum amplitude than $\delta^{18}\text{O}_{\text{wp}}$ (Figure 8c,d). The small phase offset between $\delta^{18}\text{O}_{\text{ws}}$ and $\delta^{18}\text{O}_{\text{wp}}$ likely relates to the influence of evaporation on $\delta^{18}\text{O}_{\text{ws}}$.

As found in proxy reconstructions (Cai et al., 2010; 2015; Kathayat et al., 2016) and previous modeling efforts (e.g., Kutzbach and Otto-Bliesner, 1982; Kutzbach et al., 2008), these model-reconstructed time series demonstrate that changes in precession-eccentricity are a first-order control on SASM climate. Often, these local changes in temperature and precipitation are considered drivers of $\delta^{18}\text{O}$ variability due to their strong correlations. However, we find such interpretations overly simplistic. We explore the mechanisms responsible for precession-eccentricity driven $\delta^{18}\text{O}$ changes in the SASM region below.

3.3 $\delta^{18}\text{O}$ Signals

To explore the possible causes for the precession-eccentricity driven changes in $\delta^{18}\text{O}$, we track H_2^{16}O and H_2^{18}O from their evaporative origins until their precipitation over the SASM region for SSOL and WSOL (Figure 1). We follow water evaporating from 27 different regions, which account for over 98 % of the precipitation that falls over the SASM region (see methods for details). Our results show a complex combination of sources produce the $\delta^{18}\text{O}_{\text{wp}}$ signal in the SASM region.

3.3.1 Precipitation in the SASM Region

While SSOL produces more precipitation in the SASM region than WSOL, the three greatest sources of precipitation are the same for both orbital configurations (Figure S3a,b). Ordered by contribution, these three precipitation sources include recycled water from in and around the SASM region, and water sourcing from the Arabian Sea and Southwest Indian Ocean. All three combine to contribute 47 and 63 % of the annual precipitation in SSOL and WSOL, respectively. Beyond the three main moisture sources, many differences in SASM precipitation exist between orbital configurations. The two standout differences in terms of absolute precipitation contribution to the SASM region are the Southeast Indian Ocean and North Africa sources, with each source producing over 1 mm/day more rainfall in July in SSOL than WSOL (Figure 9a,b; Figure S3c). More SASM precipitation sourcing from North Africa is a consequence of a more vigorous monsoon in that region, which leads to more evaporation that is subsequently transported east (Figure 10a-c). In contrast, the Southeast Indian Ocean precipitation source difference is largely a result of a stronger meridional flow pattern in the region in SSOL. Secondary precipitation source differences include the South Pacific Ocean and Tibet (Figure 9a,b; Figure S3c). While SSOL generally receives more precipitation in the SASM region from tagged sources, precipitation originating from the Bay of Bengal is a notable exception. Like many of the other changes in precipitation, the Bay of Bengal precipitation change relates to a shifting of the regional winds, with stronger, more northerly flow during WSOL (Figure 10b).

3.3.2 Precipitation-Weighted $\delta^{18}\text{O}$ in the SASM Region

We find that the majority of the $\delta^{18}\text{O}_{\text{wp}}$ signal comes from the summer months due to the large seasonal precipitation disparity (Figure 2; Figure 9; Figure S3d-f). Like precipitation sources, the most significant SASM $\delta^{18}\text{O}_{\text{wp}}$ sources are the same for SSOL and WSOL. The two main $\delta^{18}\text{O}_{\text{wp}}$ sources are recycling in and around the SASM region and water sourcing from Southwest Indian Ocean. The magnitude of these two $\delta^{18}\text{O}_{\text{wp}}$ signals comes mainly from their precipitation contributions to the SASM region. Water vapor sourcing from the Southeast Indian Ocean also provides a large contribution to SASM $\delta^{18}\text{O}_{\text{wp}}$ under both orbital configurations due to a combination of significant precipitation and negative $\delta^{18}\text{O}_{\text{p}}$. Other $\delta^{18}\text{O}_{\text{wp}}$ sources to the SASM region show little agreement between SSOL and WSOL.

Differencing the $\delta^{18}\text{O}_{\text{wp}}$ sources in the SASM region highlights the main contributors to the $\delta^{18}\text{O}_{\text{wp}}$ signal with changes in precession. While there are individual sources that increase the SASM $\delta^{18}\text{O}_{\text{wp}}$ signal in SSOL such as the Arabian Sea, Southwest Indian Ocean, and Bay of Bengal, the majority of sources make the SASM $\delta^{18}\text{O}_{\text{wp}}$ signal more negative, with the largest contributors coming from North Africa, Southeast Indian Ocean, and South Pacific (Figure 9c,d; Figure S3f). Overall, $\delta^{18}\text{O}_{\text{wp}}$ in the SASM region is negative in SSOL relative to WSOL, with a peak difference during July.

3.4 Mechanisms Responsible for Precipitation-Weighted $\delta^{18}\text{O}$ Change

3.4.1 Source Changes ($\Delta\delta^{18}\text{O}_{\text{source}}$)

As a whole, $\Delta\delta^{18}\text{O}_{\text{source}}$ has little effect on SASM $\Delta\delta^{18}\text{O}_{\text{wp}}$ (Figure 11b). However,

$\Delta\delta^{18}\text{O}_{\text{source}}$ from some individual regions produce important $\delta^{18}\text{O}_{\text{wp}}$ responses. For instance, $\Delta\delta^{18}\text{O}_{\text{source}}$ from North Africa and South Asia source regions produce large decreases in the $\Delta\delta^{18}\text{O}_{\text{wp}}$ signals, which relate to changes in moisture and surface temperature between SSOL and WSOL (Figure 10c,d). These negative $\Delta\delta^{18}\text{O}_{\text{wp}}$ contributions are mostly cancelled by positive $\Delta\delta^{18}\text{O}_{\text{wp}}$ contributions from $\Delta\delta^{18}\text{O}_{\text{source}}$ in the Arabian Sea, Southeast Indian Ocean, and Bay of Bengal. Here, positive $\Delta\delta^{18}\text{O}_{\text{wp}}$ relates to changes in kinetic fractionation driven by an increasing humidity, as well as slightly warmer temperatures and less local precipitation in SSOL (Figure 10b-d). While there are nontrivial differences in $\delta^{18}\text{O}$ of the sea surface water between orbits (not shown), these differences do not have a major influence on the $\delta^{18}\text{O}_{\text{wv}}$ that evaporates from the ocean surface. The disconnect between ocean surface changes in $\delta^{18}\text{O}$ and local $\delta^{18}\text{O}_{\text{wv}}$ might help explain the difference in response time of $\delta^{18}\text{O}$ between ocean and land proxies to precession-eccentricity (e.g., Ruddiman, 2006; Clemens and Prell, 2007; Clemens et al., 2010). However, this topic is beyond the scope of our current study.

3.4.2 Rainout Changes ($\Delta\delta^{18}\text{O}_{\text{rainout}}$)

$\Delta\delta^{18}\text{O}_{\text{rainout}}$ leads to a positive SASM $\Delta\delta^{18}\text{O}_{\text{wp}}$ signal, which is opposite to the negative $\Delta\delta^{18}\text{O}_{\text{wp}}$ signal found in the full SASM $\Delta\delta^{18}\text{O}_{\text{wp}}$ response (Figure 11c). This result is not unexpected. Precipitation is less in SSOL than in WSOL across the Indian ocean (Figure 3c; Figure 10a). During the spring and early summer, the South Indian Ocean and North Africa sources produce the greatest positive $\Delta\delta^{18}\text{O}_{\text{wp}}$ due to greater evaporation along the vapor transport trajectory. Later in summer and into early fall, the enhanced evaporative enrichment

along the vapor transport trajectory shifts to the Southwest Pacific, Southeast Atlantic, and Arabian Sea regions. The Tibetan Plateau is the only major region that consistently contributes to a negative $\Delta\delta^{18}\text{O}_{\text{wp}}$ signal through rainout. Across the windward side of the Plateau, greater precipitation from the enhanced monsoon strength in SSOL depletes the moisture that reaches the SASM.

3.4.3 Condensation Changes ($\Delta\delta^{18}\text{O}_{\text{condense}}$)

Previously, much of the orbital variability in speleothem $\delta^{18}\text{O}_{\text{c}}$ has been ascribed to the amount effect. In brief, the amount effect is a continual decrease in $\delta^{18}\text{O}_{\text{p}}$ with increasing rainout from a storm system. Because the heavier isotope preferentially transitions to the lower energy state, the more positive $\delta^{18}\text{O}_{\text{p}}$ precipitates first. The $\delta^{18}\text{O}_{\text{p}}$ becomes more negative as the source (cloud water vapor) becomes lighter (see Galewsky et al., 2016 for an in-depth description of the amount effect). Many studies have measured the amount effect in present-day storm events (e.g., Conroy et al., 2016). The inverse relationship between $\delta^{18}\text{O}_{\text{wp}}$ and precipitation amount in the SASM region with variations in precession-eccentricity initially appears to support the amount effect hypothesis (Figure 8).

While our model simulations show a clear amount effect signal with changes in precipitation intensity and SSOL produces more intense summer precipitation events than WSOL in the SASM region, we do not find evidence for an important amount effect signal in SASM $\delta^{18}\text{O}_{\text{wp}}$ variability (Figure 11d; Figure 12). Both orbital configurations show a similar increasing depletion response going from low to moderate daily precipitation in individual grid

cells within the SASM region. However, this relationship breaks down at high precipitation amounts. Further, there is a clear offset in the $\delta^{18}\text{O}_p$ between SSOL and WSOL; SSOL SASM $\delta^{18}\text{O}_p$ is more negative relative to WSOL for the majority of corresponding precipitation intensities, suggesting that SASM $\delta^{18}\text{O}_p$ differences are somewhat independent of precipitation intensity.

Changes in $\delta^{18}\text{O}$ between local water vapor and precipitation can be a result of many factors. Nevertheless, if the amount effect was the main driver of changes in SASM $\delta^{18}\text{O}_{wp}$ between SSOL and WSOL, we would expect to see a large $\Delta\delta^{18}\text{O}_{wp}$ response to $\Delta\delta^{18}\text{O}_{\text{condense}}$. The fact that $\Delta\delta^{18}\text{O}_{\text{condense}}$ produces only a small fraction of the actual $\Delta\delta^{18}\text{O}_{wp}$ signal supports our argument that the amount effect, and broadly, changes in precipitation processes are of low importance for understanding the SASM response (Figure 11d). Our findings support Battisti et al. (2014), who also suggest no mechanistic relationship between the changes in SASM $\delta^{18}\text{O}_{wp}$ and the amount effect despite a strong relationship between local $\delta^{18}\text{O}_{wp}$ and precipitation.

3.4.4 Relative Precipitation Contribution

The greatest contributor to SASM $\Delta\delta^{18}\text{O}_{wp}$ due to changes in precession-eccentricity comes from differences in the proportion of precipitation contributions among various water vapor sources ($\Delta\left(\frac{p_i}{p_{\text{total}}}\right)$). The SASM $\Delta\delta^{18}\text{O}_{wp}$ signal produced by $\Delta\left(\frac{p_i}{p_{\text{total}}}\right)$ matches the overall SASM $\Delta\delta^{18}\text{O}_{wp}$ signal remarkably well (Figure 11e). The three main $\Delta\left(\frac{p_i}{p_{\text{total}}}\right)$ contributors to $\Delta\delta^{18}\text{O}_{wp}$ are the Southeast Indian Ocean, South Pacific Ocean, and North Africa sources, which reflect the greatest decrease in the actual SASM $\Delta\delta^{18}\text{O}_{wp}$ signal (Figure 11a). However, there are

some discrepancies between the $\Delta\left(\frac{p_i}{p_{\text{total}}}\right)$ and actual $\Delta\delta^{18}\text{O}_{\text{wp}}$ signals, most notably in the Arabian Sea and Bay of Bengal, which show relative increases in the actual SASM $\Delta\delta^{18}\text{O}_{\text{wp}}$ signal, and in the SASM region, which shows a relative decrease in the actual SASM $\Delta\delta^{18}\text{O}_{\text{wp}}$ signal. These discrepancies result from differences in $\Delta\delta^{18}\text{O}_{\text{source}}$ instead of $\Delta\left(\frac{p_i}{p_{\text{total}}}\right)$. Nevertheless, contributions from $\Delta\left(\frac{p_i}{p_{\text{total}}}\right)$ are the dominant cause for the SASM $\Delta\delta^{18}\text{O}_{\text{wp}}$ decrease in SSOL relative to WSOL.

Changes in wind strength and direction play an important role in driving the changes in SASM relative precipitation amounts from different sources. Going from WSOL to SSOL, summer zonal winds from the west of the SASM region and Southern Hemisphere meridional winds from the southeast of the SASM region become stronger (Figure 10b). The stronger winds, in combination with a reduction in rainout, allows for a large increase in precipitation from relatively distant and isotopically depleted sources (Figure 10a).

3.5 Soil Water Signal

Weighted $\delta^{18}\text{O}$ of soil water in the top 10 cm ($\delta^{18}\text{O}_{\text{ws}}$) is more positive than $\delta^{18}\text{O}_{\text{wp}}$ due to evaporative enrichment (Figure 6; Figure 7). Further, the difference in annual SASM $\delta^{18}\text{O}_{\text{ws}}$ between SSOL and WSOL is 1.9 ‰ while for $\delta^{18}\text{O}_{\text{wp}}$ this difference is only 1.7 ‰. This enhancement in $\Delta\delta^{18}\text{O}_{\text{ws}}$ is largely driven by differences in the moisture budget. When the ratio of evaporation to precipitation increases, $\delta^{18}\text{O}_{\text{ws}}$ increases due to preferential evaporation of H_2^{16}O . While there is always more precipitation than evaporation in the SASM region during

summer, the difference between evaporation and precipitation is much smaller in WSOL than SSOL, largely due to less precipitation under similar evaporation rates (Figure 2f; Figure 5). Consequently, a greater fraction of SASM soil water evaporates during WSOL, which increases the soil water $\delta^{18}\text{O}$ signal.

3.6 Speleothem Records

There are noticeable differences in both amplitude and timing between the simulated and actual speleothem $\delta^{18}\text{O}$ signals (Figure 13). The simulated $\delta^{18}\text{O}_{\text{ws}}$ signal has greater amplitude variability compared to $\delta^{18}\text{O}_{\text{wp}}$, better matching the $\delta^{18}\text{O}_{\text{c}}$ records. Greater variability in $\delta^{18}\text{O}_{\text{ws}}$ results from surface evaporation. As mentioned above, WSOL has less rainfall than SSOL, but a similar amount of evaporation, which leads to a relatively greater effect of evaporative enrichment of ^{18}O in soil water.

In terms of timing, $\delta^{18}\text{O}_{\text{ws}}$ maxima precede the $\delta^{18}\text{O}_{\text{wp}}$ maxima by ~ 1 kyr in simulated time series at both Bittoo and Tianmen cave sites. It is difficult to determine what phasing better represents the speleothem records; noise and hiatuses in the speleothem data make model-data comparison a challenge. Further, previous modeling works found that timing of $\delta^{18}\text{O}_{\text{wp}}$ depends on the forcings considered (Caley et al., 2014); therefore, the cycles produced by precession-eccentricity forcing alone may not have the same phasing if other forcings such as ice volume, CO_2 , obliquity, and fresh water flux are included. That said, generally the local maxima and minima in the speleothem records better align with the $\delta^{18}\text{O}_{\text{wp}}$ linear reconstruction.

Adding an annual surface temperature correction to the simulated $\delta^{18}\text{O}$ time series does

not change the phasing but does decrease the amplitude slightly (Figure 13). This reduction in amplitude is a result of the relationship between the $\delta^{18}\text{O}_{\text{ws}}$ and annual mean temperature, which is warmer in WSOL than SSOL. Regardless, changes in $\delta^{18}\text{O}_c$ amplitude are fairly small, suggesting that local surface temperature is not a major driver of the SASM signal.

Despite better amplitude agreement when using $\delta^{18}\text{O}_{\text{ws}}$ for our speleothem reconstructions, we cannot confirm that including evaporative enrichment of soil water is always a better reflection of cave drip water $\delta^{18}\text{O}$. The $\delta^{18}\text{O}_c$ value ultimately deposited in a speleothem is often dependent on a variety of surface and subsurface conditions, many of which are site specific (e.g., Baker et al., 2012; Moerman et al., 2014). In fact, some studies suggest minimal evaporation of the precipitation before it enters the subsurface (Pape et al., 2009). Forward proxy modeling and cave monitoring studies are necessary next steps towards understanding these speleothem signals (Wong and Breecker, 2015).

To first order, our model simulations capture the precession frequency and phasing found in the $\delta^{18}\text{O}_c$ of the speleothem records (Figure 13). From our analyses above, we suggest this $\delta^{18}\text{O}_c$ variability relates mainly to changes in atmospheric circulation, with precession-eccentricity driven variations in monsoon strength changing the primary precipitation sources for the SASM region. For all of our reconstructions, simulated $\delta^{18}\text{O}$ amplitudes are generally smaller than the speleothem records. Underestimated Asian speleothem $\delta^{18}\text{O}$ amplitudes are a common issue for water isotope-enabled climate simulations (e.g., Laepple and Huybers, 2014, Liu et al., 2014; Battisti et al., 2014). This $\delta^{18}\text{O}$ amplitude discrepancy between the model and speleothems

could be the result of many factors beyond the scope of this work, such as model resolution and biases (Li et al., 2015; Wong et al., 2017), other climate forcings (e.g., Kutzbach et al. 2007; Caley et al., 2014), and subsurface processes (Fairchild et al., 2006; Baker et al., 2012).

Future speleothem collection at key locations could help validate the findings of this study. For example, in the northwest corner of the SASM region, the model predicts enrichment of $\delta^{18}\text{O}_{\text{wp}}$ but depletion of $\delta^{18}\text{O}_{\text{ws}}$ in SSOL relative to WSOL. Therefore, records in this location would shed light on the importance of evaporative enrichment to the $\delta^{18}\text{O}_{\text{c}}$ signal. Another location of intrigue is the southern edge of the SASM region where simulations suggest more negative $\delta^{18}\text{O}_{\text{wp}}$ with less precipitation in SSOL, highlighting the insignificance of the amount effect; speleothem records in combination with other hydrological proxies could help validate this finding. Finally, similar experiments with other isotope-enabled models are necessary to strengthen the results of this work (Risi et al., 2012).

4 Conclusions

In this study, we use a water isotope enabled version of CESM1.2 to explore $\delta^{18}\text{O}$ variability in the SASM region driven by precession-eccentricity orbital forcings. Our main findings follow:

- 1) **SASM Climate Response:** Like previous modeling studies (e.g., Kutzbach and Otto-Bliesner, 1982; Prell and Kutzbach, 1987; Kutzbach et al., 2008), our simulations suggest that summer insolation intensity is a direct driver of SASM strength. In our simulations, both the SAM index (Goswami et al., 1998) and annual precipitation over the SASM

region correlate well with Northern Hemisphere summer insolation intensity. SASM annual surface temperatures also correlate with insolation intensity. However, unlike precipitation, changes in SASM annual surface temperature result mainly from dry season insolation differences, when less cloud cover and moisture allow for more direct solar heating. Finally, weighted $\delta^{18}\text{O}$ of precipitation ($\delta^{18}\text{O}_{\text{wp}}$) and soil moisture ($\delta^{18}\text{O}_{\text{ws}}$) show a strong negative correlation with summer insolation and SASM intensity. A strong SASM corresponds with more negative local $\delta^{18}\text{O}$ and vice versa, as found in prior modeling efforts (Pausata et al., 2011; Liu et al., 2014; Battisti et al., 2014; Caley et al., 2014). Because of the large seasonal disparity in precipitation, summer dominates the $\delta^{18}\text{O}_{\text{wp}}$ signal in the SASM region.

- 2) **Causes of SASM $\delta^{18}\text{O}$ Variability:** We are able to deconstruct the contributions to precession-eccentricity driven SASM $\delta^{18}\text{O}_{\text{wp}}$ variability by separating the signals into multiple water source regions. In the model, changes in the $\delta^{18}\text{O}$ of water vapor ($\delta^{18}\text{O}_{\text{wv}}$) from regions that source SASM precipitation contribute minimally to the $\delta^{18}\text{O}_{\text{wp}}$ response to variations in precession-eccentricity. Likewise, changes in the conversion from water vapor to precipitation in the SASM region with changes in precession-eccentricity have little impact on the SASM $\delta^{18}\text{O}_{\text{wp}}$ signal. Therefore, as found in previous works, it is unlikely that the amount effect is responsible for the SASM $\delta^{18}\text{O}_{\text{wp}}$ signal, despite a correlation between precipitation amount and $\delta^{18}\text{O}_{\text{wp}}$ (Pausata et al., 2011; Battisti et al., 2014). Further, $\delta^{18}\text{O}_{\text{wp}}$ changes due to rainout along the transport trajectory contribute

adversely to the simulated $\delta^{18}\text{O}_{\text{wp}}$ signal in the SASM region. Instead, we find that the majority of the SASM $\delta^{18}\text{O}_{\text{wp}}$ decrease in SSOL relative to WSOL comes from fractional changes of various vapor sources contributing to the SASM precipitation. Water vapor tends to source from farther away during the strong monsoons created by high Northern Hemisphere summer insolation orbits. In general, distant water vapor sources are more depleted by the time they reach the SASM region due to precipitation during transport. Therefore, a greater proportion of water vapor sourcing from these distant regions during SSOL compared to WSOL leads to a more negative SASM $\delta^{18}\text{O}_{\text{wp}}$ signal.

- 3) **SASM Speleothem Signals:** Climate models often have difficulty replicating the amplitude of $\delta^{18}\text{O}_{\text{c}}$ variability found in speleothem records with simulated $\delta^{18}\text{O}_{\text{wp}}$ (e.g., Liu et al., 2014; Battisti et al., 2014). We suggest that $\delta^{18}\text{O}_{\text{ws}}$ may better reflect the $\delta^{18}\text{O}$ of soil water that enters the karst (Dee et al., 2015). Relative to $\delta^{18}\text{O}_{\text{wp}}$, 10-cm SASM $\delta^{18}\text{O}_{\text{ws}}$ produces an amplified precession-eccentricity signal, which better matches speleothem records (Cai et al., 2010; 2015; Kathayat et al., 2016). Amplified $\delta^{18}\text{O}$ variability in soil water is a consequence of surface evaporation. During SSOL, the climate is fairly wet, resulting in a large precipitation to evaporation ratio, which decreases $\delta^{18}\text{O}_{\text{ws}}$. Conversely, during WSOL, the ratio of precipitation to evaporation is smaller, due in large part to a reduction in precipitation. In this orbit, the water vapor that remains in the soil becomes heavier due to a relatively greater amount of evaporation, which enhances the overall enrichment signal of WSOL.

In summary, variability in $\delta^{18}\text{O}_c$ of SASM speleothems forced by changes in insolation due to cycles of precession-eccentricity can be considered primarily a proxy for summer monsoon intensity. Our simulations suggest that these variations in SASM $\delta^{18}\text{O}$ come from a combination of changes in the relative amount of precipitation sourced from distant locations and local evaporation. Although $\delta^{18}\text{O}_{\text{wp}}$ and precipitation show an inverse relationship over much of the SASM region with cycles of precession-eccentricity, $\delta^{18}\text{O}_{\text{wp}}$ variability is not a direct response to changes in precipitation amount. This work helps explain the mechanisms responsible for precession-driven variability found in SASM $\delta^{18}\text{O}_c$ and highlights the need for model simulations to better interpret long term isotopic records.

Figure 1. Tagged water vapor regions for tracking moisture sources to the SASM region. **a)** Blue boxes define tags that track moisture evaporating from ocean only. **b)** Red boxes define tags that track moisture evaporating from land only, and purple boxes define tags that track moisture evaporating from both land and ocean. Stars mark Bittoo (Kathayat et al., 2016) and Tianmen (Cai et al., 2010) speleothem locations.

Figure 2. Monthly climatologies from different configurations of precession-eccentricity in the SASM region (10° – 30°N and 70° – 100°E). **a)** Top of atmosphere incoming insolation, **b)** $\delta^{18}\text{O}$ of precipitation, **c)** $\delta^{18}\text{O}$ of top 10 cm soil water, **d)** surface evaporation, **e)** total precipitation, **f)** difference between evaporation and precipitation, **g)** surface temperature, **h)** 900 hPa equivalent potential temperature (\square_c), **i)** SAM index (difference in the meridional winds between 850 and

250 hPa and from 10°–30°N and 70°–110°E; Goswami et al., 1998).

Figure 3. Climatology of JJAS precipitation and 850 hPa winds in a high eccentricity orbit with perihelion at the Northern Hemisphere **a)** winter solstice (WSOL), **b)** summer solstice (SSOL), and **c)** their difference. Interior box outlines the SASM region.

Figure 4. Climatology of JJAS surface temperature in a high eccentricity orbit with perihelion at the Northern Hemisphere **a)** winter solstice (WSOL), **b)** summer solstice (SSOL), and **c)** their difference. Interior box outlines the SASM region.

Figure 5. Climatology of JJAS surface evaporation in a high eccentricity orbit with perihelion at the Northern Hemisphere **a)** winter solstice (WSOL), **b)** summer solstice (SSOL), and **c)** their difference. Interior box outlines the SASM region.

Figure 6. Climatology of annual weighted $\delta^{18}\text{O}$ of precipitation in a high eccentricity orbit with perihelion at the Northern Hemisphere **a)** winter solstice (WSOL), **b)** summer solstice (SSOL), and **c)** their difference. Interior box outlines the SASM region. Stars mark Bittoo and Tianmen speleothem locations.

Figure 7. Climatology of annual $\delta^{18}\text{O}$ of soil water in the top 10 cm in a high eccentricity orbit with perihelion at Northern Hemisphere **a)** winter solstice (WSOL), **b)** summer solstice (SSOL), and **c)** their difference. Interior box outlines the SASM region. Stars mark Bittoo and Tianmen speleothem locations.

Figure 8. Model-based reconstructions of annual mean climate anomalies in the SASM region for the past 250 ka using linear combinations of the precession-eccentricity forcings. **a)** Total

precipitation, **b**) Surface temperature, **c**) Weighted $\delta^{18}\text{O}$ of precipitation, **d**) Weighted $\delta^{18}\text{O}$ of soil water in the top 10 cm. Red dashed line traces June insolation anomalies from linear combinations of precession-eccentricity averaged over the same SASM domain. Note that the y-axis for surface temperature and $\delta^{18}\text{O}$ are inverted.

Figure 9. Differences in annual average precipitation (mm/day) in the SASM region between SSOL and WSOL from different moisture sources over **a**) ocean and **b**) land. For precipitation, blue values are positive and red values are negative. Differences in annual weighted $\delta^{18}\text{O}$ of precipitation (‰) between SSOL and WSOL from different moisture sources over **c**) ocean and **d**) land. For $\delta^{18}\text{O}$, blue values are negative and red values are positive. Yellow shading identifies the top 5 source region differences for precipitation and $\delta^{18}\text{O}$ in terms of magnitude.

Figure 10. JJAS climatological differences between simulations with perihelion during the Northern Hemisphere summer (SSOL) and winter (WSOL) solstices. **a**) Precipitation differences, **b**) near surface winds and 10 m wind magnitude differences, **c**) evaporation differences, and **d**) surface temperature differences. Interior box outlines the SASM region.

Figure 11. The impact of various phenomena on the weighted $\delta^{18}\text{O}$ of precipitation change in the SASM region between perihelion during the Northern Hemisphere summer (SSOL) and winter (WSOL) solstices. **a**) The actual difference in weighted $\delta^{18}\text{O}$ of precipitation between SSOL and WSOL, showing the total as well as terms corresponding to water vapor source regions. The difference in weighted $\delta^{18}\text{O}$ of precipitation between SSOL and WSOL that results from changes in: **b**) $\delta^{18}\text{O}$ of water vapor at their sources, **c**) rainout of water vapor between the sources and

SASM region, **d**) the transition from water vapor to precipitation over the SASM region, and **e**) the amount of precipitation coming from different water sources. The left y-axis corresponds with individual water sources and the right y-axis corresponds to total signal (thick black line).

Figure 12. Relationship between daily precipitation amounts and $\delta^{18}\text{O}$ of precipitation at individual grid cells and the cumulative distribution function (CDF) of precipitation using the final 20 years of simulation. Left y-axis: $\delta^{18}\text{O}$ of precipitation. Right y-axis: percent of total distribution.

Figure 13. Comparing $\delta^{18}\text{O}$ of calcium carbonate from speleothems with model reconstructions of $\delta^{18}\text{O}$ from precession-eccentricity cycles using linear combinations. Modeled reconstructions of weighted $\delta^{18}\text{O}$ of precipitation (green lines), top 10 cm soil water (purple lines), and soil water with a cave temperature correction (orange lines) compared against **a**) the Bittoo cave ($30^{\circ}47'\text{N}$; $77^{\circ}47'\text{E}$) record (Kathayat et al., 2016) and **b**) Tianmen cave ($30^{\circ}55'\text{N}$; $90^{\circ}4'\text{E}$) record (Cai et al., 2010). Thick black lines: cave records interpolated to 1 kyr intervals. Red dashed lines: low pass filtered cave records with a 20 kyr cut-off frequency using Lanczos filtering. Means have been removed from all data for comparison.

References

Ashfaq, M., Rastogi, D., Mei, R., Touma, D., & Leung, L. R. (2016). Sources of errors in the simulation of south Asian summer monsoon in the CMIP5 GCMs. *Climate Dynamics*, 49(1-2), 193-223.

- Battisti, D. S., Ding, Q., & Roe, G. H. (2014). Coherent pan-Asian climatic and isotopic response to orbital forcing of tropical insolation. *Journal of Geophysical Research: Atmospheres*, *119*(21).
- Baker, A., Bradley, C., Phipps, S. J., Fischer, M., Fairchild, I. J., Fuller, L., et al. (2012). Millennial-length forward models and pseudoproxies of stalagmite $\delta^{18}O$: an example from NW Scotland. *Climate of the Past*, *8*(4), 1153.
- Berger, A., & Loutre, M. F. (1991). Insolation values for the climate of the last 10 million years. *Quaternary Science Reviews*, *10*(4), 297-317.
- Boos, W. R., & Kuang, Z. (2010). Dominant control of the South Asian monsoon by orographic insolation versus plateau heating. *Nature*, *463*(7278), 218.
- Boos, W. R. (2015). A review of recent progress on Tibet's role in the South Asian monsoon. *CLIVAR Exch*, *19*, 23-27.
- Bosmans, J. H. C., Erb, M. P., Dolan, A. M., Drijfhout, S. S., Tuenter, E., Hilgen, F. J., ... & Lourens, L. J. (2018). Response of the Asian summer monsoons to idealized precession and obliquity forcing in a set of GCMs. *Quaternary Science Reviews*, *188*, 121-135.
- Braconnot, P., Marzin, C., Grégoire, L., Mosquet, E., & Marti, O. (2008). Monsoon response to changes in Earth's orbital parameters: comparisons between simulations of the Eemian and of the Holocene. *Climate of the Past*, *4*(2), 459-493.

- Cai, Y., An, Z., Cheng, H., Edwards, R. L., Kelly, M. J., Liu, W., et al. (2006). High-resolution absolute-dated Indian Monsoon record between 53 and 36 ka from Xiaobailong Cave, southwestern China. *Geology*, *34*(8), 621-624.
- Cai, Y., Cheng, H., An, Z., Edwards, R. L., Wang, X., Tan, L., & Wang, J. (2010). Large variations of oxygen isotopes in precipitation over south-central Tibet during Marine Isotope Stage 5. *Geology*, *38*(3), 243-246.
- Cai, Y., Fung, I. Y., Edwards, R. L., An, Z., Cheng, H., Lee, J. E., et al. (2015). Variability of stalagmite-inferred Indian monsoon precipitation over the past 252,000 y. *Proceedings of the National Academy of Sciences*, *112*(10), 2954-2959.
- Caley, T., Roche, D. M., & Renssen, H. (2014). Orbital Asian summer monsoon dynamics revealed using an isotope-enabled global climate model. *Nature communications*, *5*, 5371.
- Chakraborty, A. N. R. S., Nanjundiah, R. S., & Srinivasan, J. (2006, September). Theoretical aspects of the onset of Indian summer monsoon from perturbed orography simulations in a GCM. In *Annales Geophysicae* (Vol. 24, No. 8, p. 2075). SPRINGER VERLAG KG.
- Chen, G. S., Liu, Z., & Kutzbach, J. E. (2014). Reexamining the barrier effect of the Tibetan Plateau on the South Asian summer monsoon. *Climate of the Past*, *10*(3), 1269-1275.
- Cheng, H., Zhang, P. Z., Spötl, C., Edwards, R. L., Cai, Y. J., Zhang, D. Z., et al. (2012). The climatic cyclicity in semiarid-arid central Asia over the past 500,000 years. *Geophysical Research Letters*, *39*(1).

- Cheng, H., Edwards, R. L., Sinha, A., Spötl, C., Yi, L., Chen, S., et al. (2016). The Asian monsoon over the past 640,000 years and ice age terminations. *Nature*, *534*(7609), 640.
- Clemens, S., Prell, W., Murray, D., Shimmield, G., & Weedon, G. (1991). Forcing mechanisms of the Indian Ocean monsoon. *Nature*, *353*(6346), 720.
- Clemens, S. C., & Prell, W. L. (2007). The timing of orbital-scale Indian monsoon changes. *Quaternary Science Reviews*, *26*(3-4), 275-278.
- Clemens, S. C., Prell, W. L., & Sun, Y. (2010). Orbital-scale timing and mechanisms driving Late Pleistocene Indo-Asian summer monsoons: Reinterpreting cave speleothem $\delta^{18}\text{O}$. *Paleoceanography*, *25*(4).
- Conroy, J. L., Noone, D., Cobb, K. M., Moerman, J. W., & Konecky, B. L. (2016). Paired stable isotopologues in precipitation and vapor: A case study of the amount effect within western tropical Pacific storms. *Journal of Geophysical Research: Atmospheres*, *121*(7), 3290-3303.
- Dansgaard, W. (1964). Stable isotopes in precipitation. *Tellus*, *16*(4), 436-468.
- Dee, S., Emile-Geay, J., Evans, M. N., Allam, A., Steig, E. J., & Thompson, D. M. (2015). PRYSM: An open-source framework for PRoxY System Modeling, with applications to oxygen-isotope systems. *Journal of Advances in Modeling Earth Systems*, *7*(3), 1220-1247.
- Erb, M. P., Jackson, C. S., & Broccoli, A. J. (2015). Using single-forcing GCM simulations to reconstruct and interpret Quaternary climate change. *Journal of Climate*, *28*, 9746-9767.

- Fairchild, I. J., Smith, C. L., Baker, A., Fuller, L., Spötl, C., Matthey, D., & McDermott, F. (2006). Modification and preservation of environmental signals in speleothems. *Earth-Science Reviews*, 75(1-4), 105-153.
- Fasullo, J., & Webster, P. J. (2003). A hydrological definition of Indian monsoon onset and withdrawal. *Journal of Climate*, 16(19), 3200-3211.
- Feng, R., Li, J., & Wang, J. (2011). Regime change of the boreal summer Hadley circulation and its connection with the tropical SST. *Journal of Climate*, 24(15), 3867-3877.
- Feng, R., Poulsen, C. J., Werner, M., Chamberlain, C. P., Mix, H. T., & Mulch, A. (2013). Early Cenozoic evolution of topography, climate, and stable isotopes in precipitation in the North American Cordillera. *American Journal of Science*, 313(7), 613-648.
- Feng, R., Poulsen, C. J., & Werner, M. (2016). Tropical circulation intensification and tectonic extension recorded by Neogene terrestrial $\delta^{18}\text{O}$ records of the western United States. *Geology*, 44(11), 971-974.
- Friedman, I., & O'Neil, J. R. (1977). *Data of geochemistry: Compilation of stable isotope fractionation factors of geochemical interest* (Vol. 440). US Government Printing Office.
- Gadgil, S. (2003). The Indian monsoon and its variability. *Annual Review of Earth and Planetary Sciences*, 31(1), 429-467.
- Galewsky, J., Steen-Larsen, H. C., Field, R. D., Worden, J., Risi, C., & Schneider, M. (2016). Stable isotopes in atmospheric water vapor and applications to the hydrologic cycle. *Reviews of Geophysics*, 54(4), 809-865.

- Goswami, B. N., Krishnamurthy, V., & Annmalai, H. (1999). A broad-scale circulation index for the interannual variability of the Indian summer monsoon. *Quarterly Journal of the Royal Meteorological Society*, *125*(554), 611-633.
- He, H., McGinnis, J. W., Song, Z., & Yanai, M. (1987). Onset of the Asian summer monsoon in 1979 and the effect of the Tibetan Plateau. *Monthly Weather Review*, *115*(9), 1966-1995.
- Huffman, G. J., & Bolvin, D. T. (2013). TRMM and other data precipitation data set documentation. *NASA, Greenbelt, USA*, 28.
- Hurrell, J. W., Holland, M. M., Gent, P. R., Ghan, S., Kay, J. E., Kushner, P. J., et al. (2013). The community earth system model: a framework for collaborative research. *Bulletin of the American Meteorological Society*, *94*(9), 1339-1360.
- Iguchi, T., Kozu, T., Kwiatkowski, J., Meneghini, R., Awaka, J., & Okamoto, K. I. (2009). Uncertainties in the rain profiling algorithm for the TRMM precipitation radar. *Journal of the Meteorological Society of Japan. Ser. II*, *87*, 1-30.
- Joussaume, S., & Braconnot, P. (1997). Sensitivity of paleoclimate simulation results to season definitions. *Journal of Geophysical Research: Atmospheres*, *102*(D2), 1943-1956.
- Kathayat, G., Cheng, H., Sinha, A., Spötl, C., Edwards, R. L., Zhang, H., et al. (2016). Indian monsoon variability on millennial-orbital timescales. *Scientific Reports*, *6*, 24374.
- Kutzbach, J. E., & Otto-Bliesner, B. L. (1982). The sensitivity of the African-Asian monsoonal climate to orbital parameter changes for 9000 years BP in a low-resolution general circulation model. *Journal of the Atmospheric Sciences*, *39*(6), 1177-1188.

- Kutzbach, J. E., Liu, X., Liu, Z., & Chen, G. (2008). Simulation of the evolutionary response of global summer monsoons to orbital forcing over the past 280,000 years. *Climate Dynamics*, 30(6), 567-579.
- Laepple, T., & Huybers, P. (2014). Ocean surface temperature variability: Large model–data differences at decadal and longer periods. *Proceedings of the National Academy of Sciences*, 111(47), 16682-16687.
- Le Mézo, P., Beaufort, L., Bopp, L., Braconnot, P., & Kageyama, M. (2017). From monsoon to marine productivity in the Arabian Sea: insights from glacial and interglacial climates. *Climate of the Past*, 13(7), 759.
- LeGrande, A. N., & Schmidt, G. A. (2006). Global gridded data set of the oxygen isotopic composition in seawater. *Geophysical research letters*, 33(12).
- Li, C., & Yanai, M. (1996). The onset and interannual variability of the Asian summer monsoon in relation to land–sea thermal contrast. *Journal of Climate*, 9(2), 358-375.
- Li, J., Yu, R., Yuan, W., Chen, H., Sun, W., & Zhang, Y. (2015). Precipitation over East Asia simulated by NCAR CAM5 at different horizontal resolutions. *Journal of Advances in Modeling Earth Systems*, 7(2), 774-790.
- Liu, Z., Otto-Bliesner, B., Kutzbach, J., Li, L., & Shields, C. (2003). Coupled climate simulation of the evolution of global monsoons in the Holocene. *Journal of Climate*, 16(15), 2472-2490.

- Liu, Z., Wen, X., Brady, E. C., Otto-Bliesner, B., Yu, G., Lu, H., et al. (2014). Chinese cave records and the East Asia summer monsoon. *Quaternary Science Reviews*, 83, 115-128.
- McDermott, F. (2004). Palaeo-climate reconstruction from stable isotope variations in speleothems: a review. *Quaternary Science Reviews*, 23(7-8), 901-918.
- Meehl, G. A., Arblaster, J. M., Caron, J. M., Annamalai, H., Jochum, M., Chakraborty, A., & Murtugudde, R. (2012). Monsoon regimes and processes in CCSM4. Part I: The Asian–Australian monsoon. *Journal of Climate*, 25(8), 2583-2608.
- Meehl, G. A., Washington, W. M., Arblaster, J. M., Hu, A., Teng, H., Kay, J. E., et al. (2013). Climate change projections in CESM1 (CAM5) compared to CCSM4. *Journal of Climate*, 26(17), 6287-6308.
- Moerman, J. W., Cobb, K. M., Partin, J. W., Meckler, A. N., Carolin, S. A., Adkins, J. F., et al. (2014). Transformation of ENSO-related rainwater to dripwater $\delta^{18}\text{O}$ variability by vadose water mixing. *Geophysical Research Letters*, 41(22), 7907-7915.
- Molnar, P., Boos, W. R., & Battisti, D. S. (2010). Orographic controls on climate and paleoclimate of Asia: thermal and mechanical roles for the Tibetan Plateau. *Annual Review of Earth and Planetary Sciences*, 38.
- Nusbaumer, J., Wong, T. E., Bardeen, C., & Noone, D. (2017). Evaluating hydrological processes in the Community Atmosphere Model Version 5 (CAM5) using stable isotope ratios of water. *Journal of Advances in Modeling Earth Systems*, 9(2), 949-977.

- Pape, J. R., Banner, J. L., Mack, L. E., Musgrove, M., & Guilfoyle, A. (2010). Controls on oxygen isotope variability in precipitation and cave drip waters, central Texas, USA. *Journal of Hydrology*, 385(1-4), 203-215.
- Pausata, F. S., Battisti, D. S., Nisancioglu, K. H., & Bitz, C. M. (2011). Chinese stalagmite $\delta^{18}\text{O}$ controlled by changes in the Indian monsoon during a simulated Heinrich event. *Nature Geoscience*, 4(7), 474.
- Plumb, R. A., & Hou, A. Y. (1992). The response of a zonally symmetric atmosphere to subtropical thermal forcing: Threshold behavior. *Journal of the atmospheric sciences*, 49(19), 1790-1799.
- Pollard, D., & Reusch, D. B. (2002). A calendar conversion method for monthly mean paleoclimate model output with orbital forcing. *Journal of Geophysical Research: Atmospheres*, 107(D22).
- Poulsen, C. J., Ehlers, T. A., & Insel, N. (2010). Onset of convective rainfall during gradual late Miocene rise of the central Andes. *science*, 328(5977), 490-493.
- Prell, W. L., & Kutzbach, J. E. (1987). Monsoon variability over the past 150,000 years. *Journal of Geophysical Research: Atmospheres*, 92(D7), 8411-8425.
- Privé, N. C., & Plumb, R. A. (2007). Monsoon dynamics with interactive forcing. Part I: Axisymmetric studies. *Journal of the atmospheric sciences*, 64(5), 1417-1430.

- Privé, N. C., & Plumb, R. A. (2007). Monsoon dynamics with interactive forcing. Part II: Impact of eddies and asymmetric geometries. *Journal of the atmospheric sciences*, *64*(5), 1431-1442.
- Risi, C., Noone, D., Worden, J., Frankenberg, C., Stiller, G., Kiefer, M., et al. (2012). Process-evaluation of tropospheric humidity simulated by general circulation models using water vapor isotopologues: 1. Comparison between models and observations. *Journal of Geophysical Research: Atmospheres*, *117*(D5).
- Roe, G. H., Ding, Q., Battisti, D. S., Molnar, P., Clark, M. K., & Garzione, C. N. (2016). A modeling study of the response of Asian summertime climate to the largest geologic forcings of the past 50 Ma. *Journal of Geophysical Research: Atmospheres*, *121*(10), 5453-5470.
- Ruddiman, W. F. (2006). What is the timing of orbital-scale monsoon changes?. *Quaternary Science Reviews*, *25*(7-8), 657-658.
- Sperber, K. R., Annamalai, H., Kang, I. S., Kitoh, A., Moise, A., Turner, A., et al. (2013). The Asian summer monsoon: an intercomparison of CMIP5 vs. CMIP3 simulations of the late 20th century. *Climate Dynamics*, *41*(9-10), 2711-2744.
- Tabor, C. R., Poulsen, C. J., & Pollard, D. (2014). Mending Milankovitch's theory: obliquity amplification by surface feedbacks. *Climate of the Past*, *10*(1), 41-50.

- Tabor, C. R., Poulsen, C. J., & Pollard, D. (2015). How obliquity cycles powered early Pleistocene global ice-volume variability. *Geophysical Research Letters*, *42*(6), 1871-1879.
- Tuenter, E., Weber, S. L., Hilgen, F. J., Lourens, L. J., & Ganopolski, A. (2005). Simulation of climate phase lags in response to precession and obliquity forcing and the role of vegetation. *Climate Dynamics*, *24*(2-3), 279-295.
- Vuille, M., Werner, M., Bradley, R. S., & Keimig, F. (2005). Stable isotopes in precipitation in the Asian monsoon region. *Journal of Geophysical Research: Atmospheres*, *110*(D23).
- Wang, Y., Cheng, H., Edwards, R. L., Kong, X., Shao, X., Chen, S., et al. (2008). Millennial-and orbital-scale changes in the East Asian monsoon over the past 224,000 years. *Nature*, *451*(7182), 1090.
- Webster, P. J., & Yang, S. (1992). Monsoon and ENSO: Selectively interactive systems. *Quarterly Journal of the Royal Meteorological Society*, *118*(507), 877-926.
- Webster, P. J., Magana, V. O., Palmer, T. N., Shukla, J., Tomas, R. A., Yanai, M. U., & Yasunari, T. (1998). Monsoons: Processes, predictability, and the prospects for prediction. *Journal of Geophysical Research: Oceans*, *103*(C7), 14451-14510.
- Wong, C. I., & Breecker, D. O. (2015). Advancements in the use of speleothems as climate archives. *Quaternary Science Reviews*, *127*, 1-18.
- Wong, T. E., Nusbaumer, J., & Noone, D. C. (2017). Evaluation of modeled land-atmosphere exchanges with a comprehensive water isotope fractionation scheme in version 4 of the

Community Land Model. *Journal of Advances in Modeling Earth Systems*, 9(2), 978-1001.

Wu, G., Liu, Y., He, B., Bao, Q., Duan, A., & Jin, F. F. (2012). Thermal controls on the Asian summer monsoon. *Scientific reports*, 2, 404.

Yanai, M., & Wu, G. X. (2006). Effects of the tibetan plateau. In *The Asian Monsoon* (pp. 513-549). Springer, Berlin, Heidelberg.

Zhang, J., Liu, Z., Brady, E. C., Oppo, D. W., Clark, P. U., Jahn, A., et al. (2017). Asynchronous warming and $\delta^{18}\text{O}$ evolution of deep Atlantic water masses during the last deglaciation. *Proceedings of the National Academy of Sciences*, 201704512.

Zhu, J., Liu, Z., Brady, E., Otto-Bliesner, B., Zhang, J., Noone, D., et al. (2017). Reduced ENSO Variability at the LGM Revealed by an Isotope-enabled Earth System Model. *Geophysical Research Letters*.

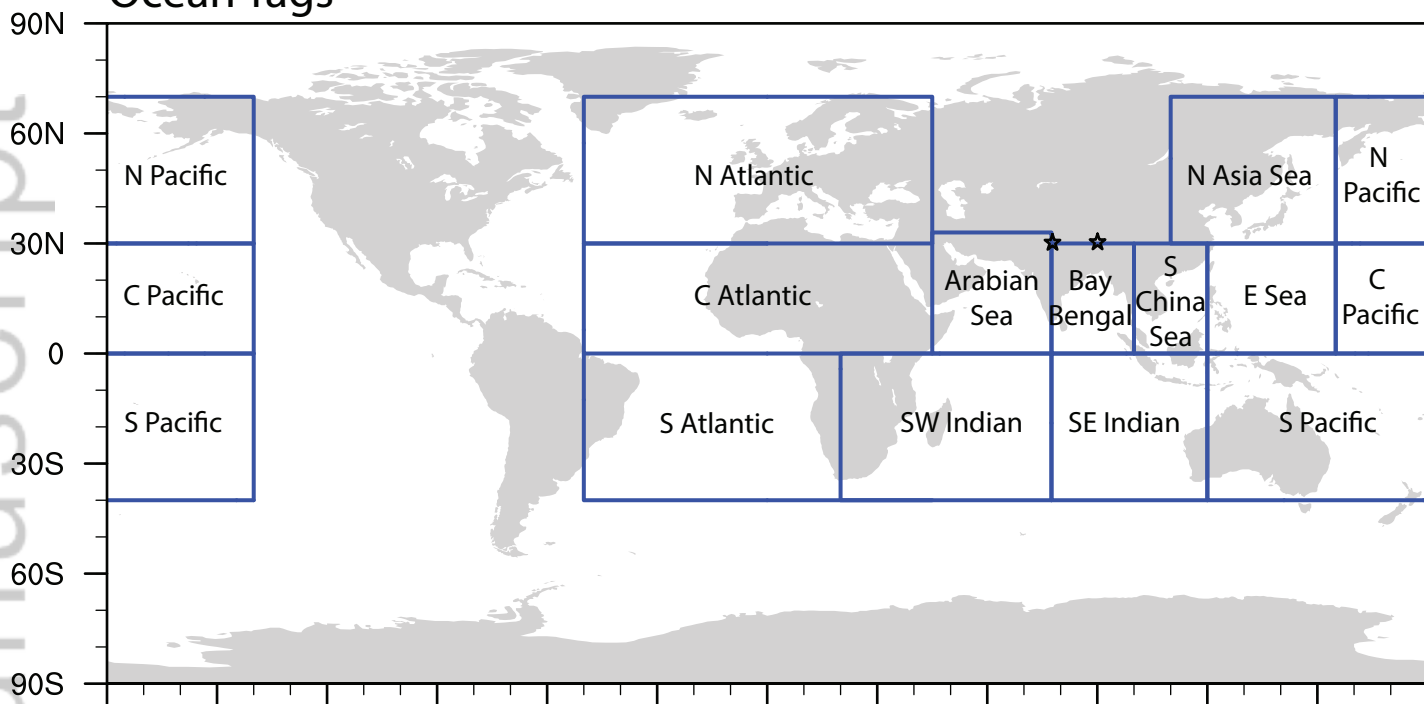
Ziegler, M., Tuenter, E., & Lourens, L. J. (2010). The precession phase of the boreal summer monsoon as viewed from the eastern Mediterranean (ODP Site 968). *Quaternary Science Reviews*, 29(11), 1481-1490.

Acknowledgements

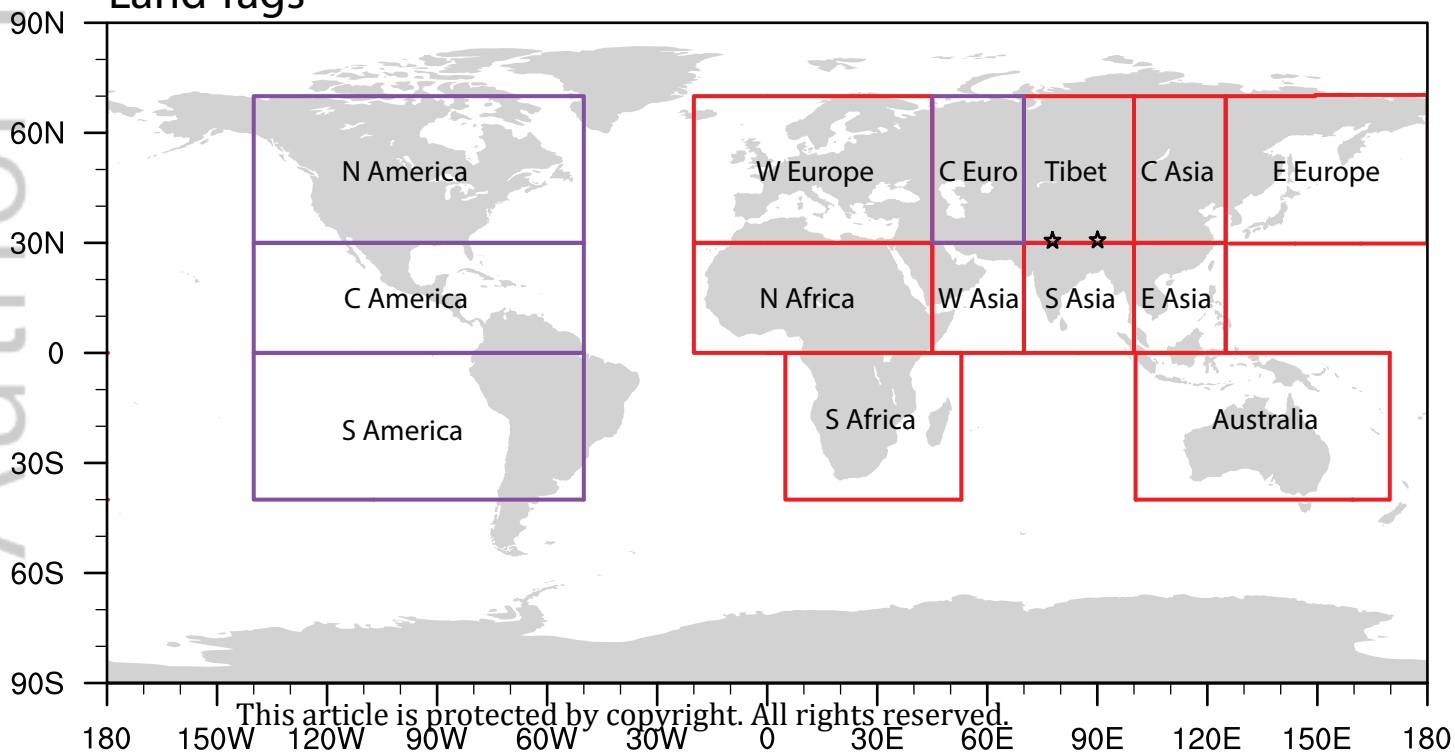
This work was improved by the thoughtful comments of two anonymous reviewers. Development of the stable water isotope-enabled version of the Community Earth System Model was made possible by the National Science Foundation (NSF) grants AGS-1401778, AGS-

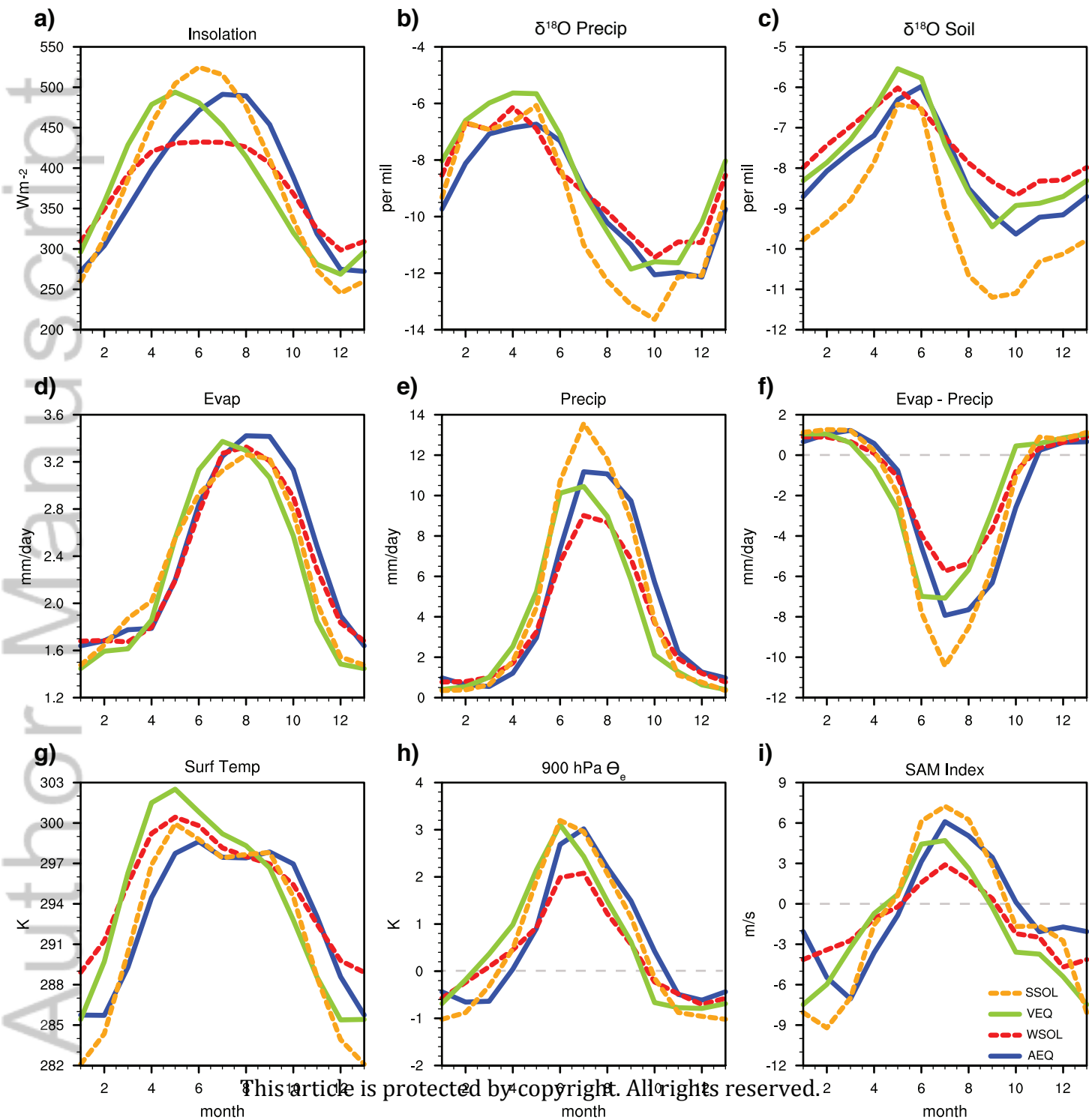
1401803, and AGS-1401802. Clay Tabor acknowledges funding from the National Center for Atmospheric Research (NCAR) Advanced Study Program (ASP) postdoctoral fellowship and the computational resources provided by the NCAR Strategic Capability (NSC) project run by Computational and Information Systems Lab (CISL). We would like to acknowledge high-performance computing support from Yellowstone (ark:/85065/d7wd3xhc) provided by NCAR's CISL, sponsored by NSF. The iCESM model codes are available through the NCAR software development repository. Data presented in this manuscript are stored on the NCAR server and available by email request to Clay Tabor (clay.tabor@uconn.edu).

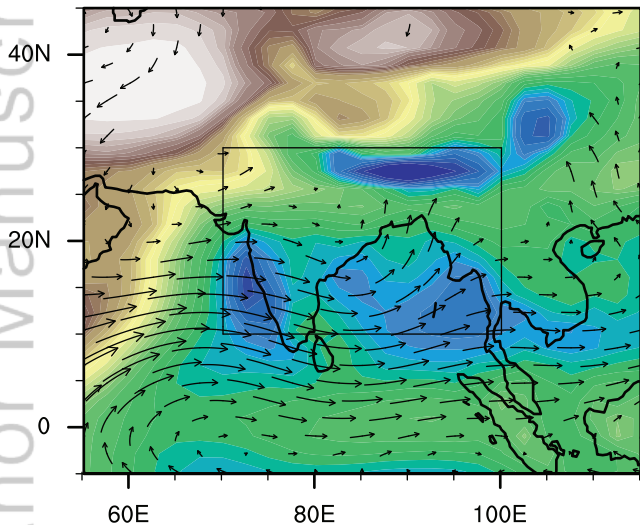
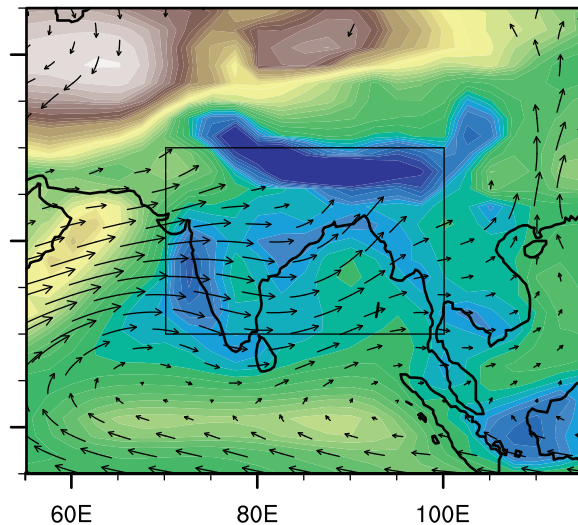
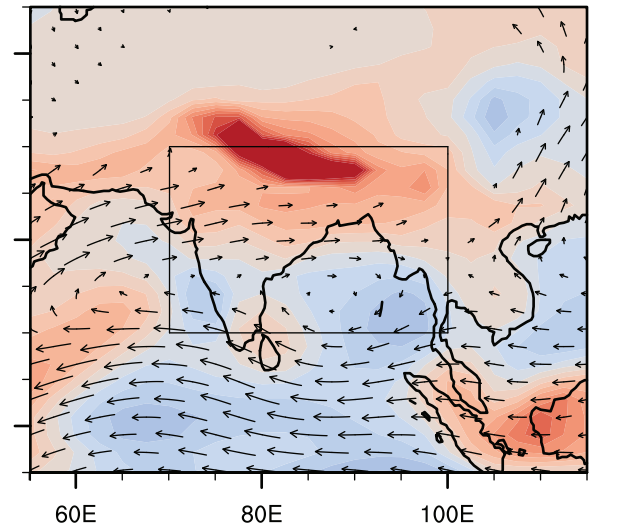
a) Ocean Tags



b) Land Tags



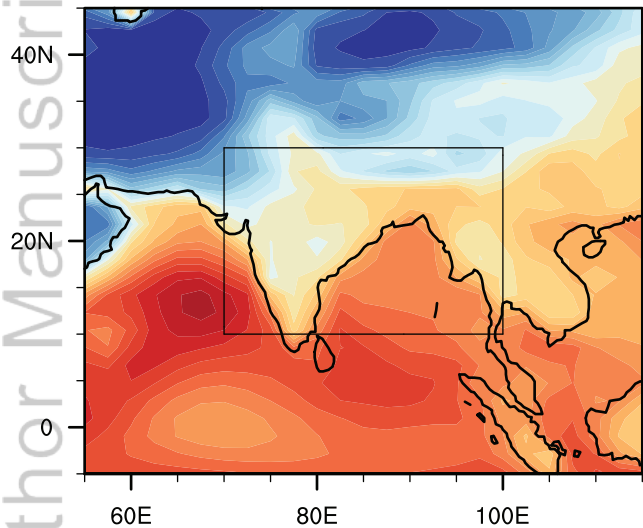


a) JJAS Precip and 850 hPa Wind: WSOL**b)** JJAS Precip and 850 hPa Wind: SSOL**c)** JJAS Precip and 850 hPa Wind: SSOL - WSOL

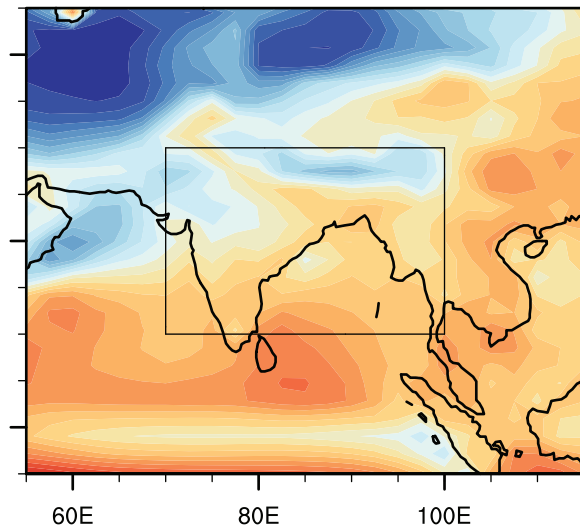
This article is protected by copyright. All rights reserved.

a)

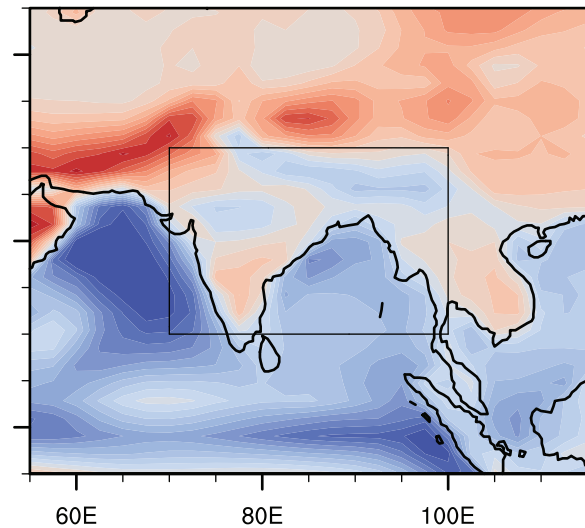
JJAS Surf Evap: WSOL

**b)**

JJAS Surf Evap: SSOL

**c)**

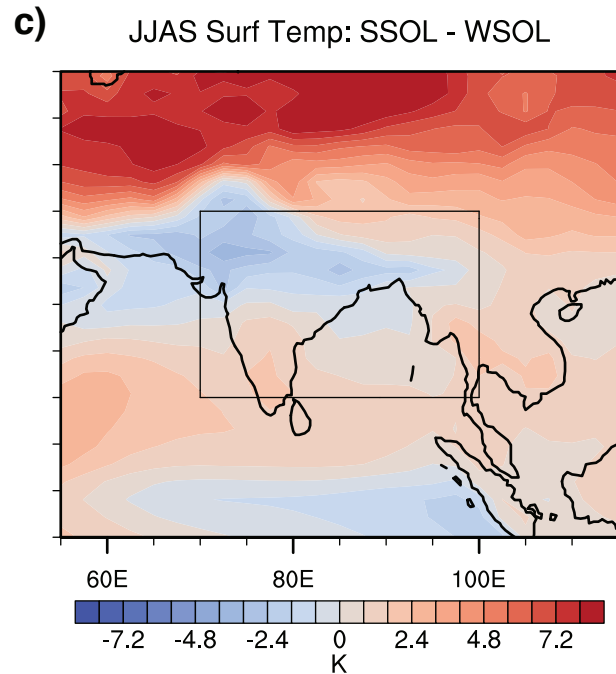
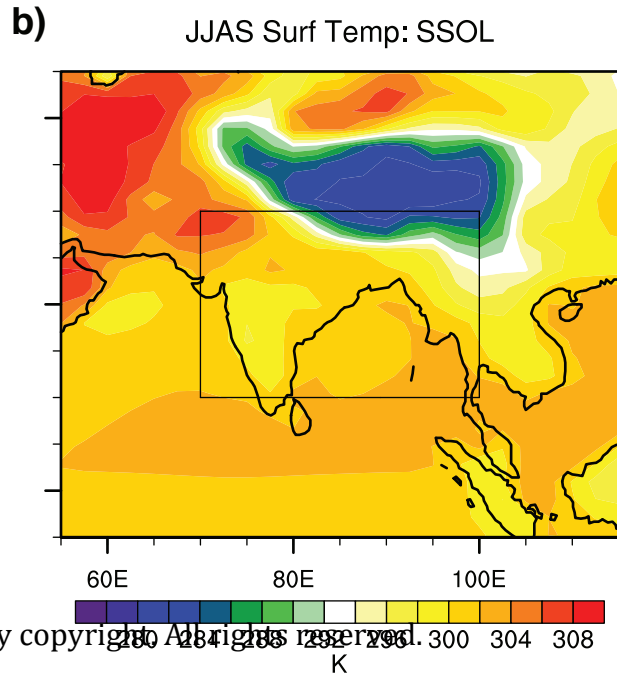
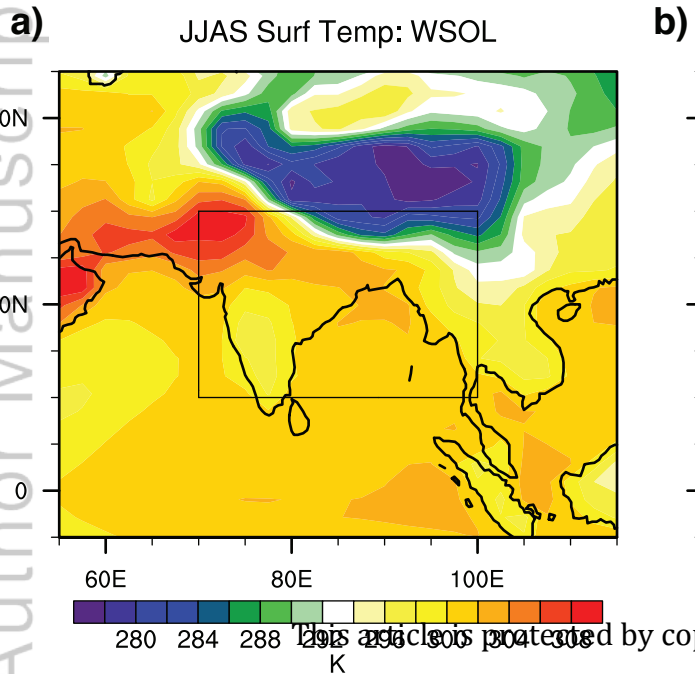
JJAS Surf Evap: SSOL - WSOL

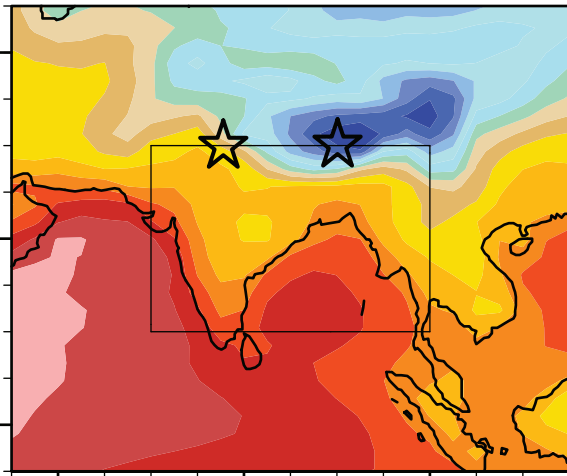


0.5 1 1.5 2 2.5 3 3.5 4 4.5 5 5.5 6
mm/day

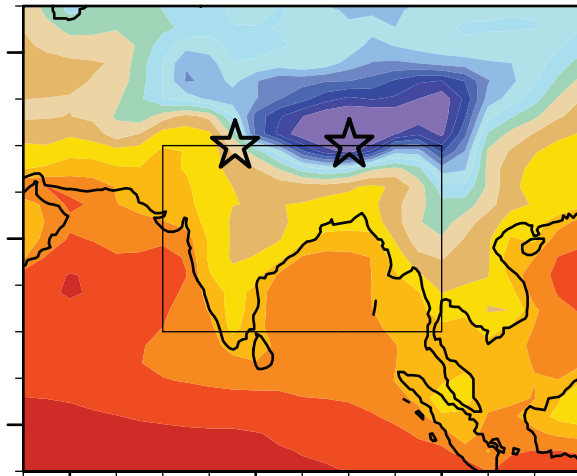
0.5 1 1.5 2 2.5 3 3.5 4 4.5 5 5.5 6
mm/day

-1.8 -1.2 -0.6 0 0.6 1.2 1.8
mm/day

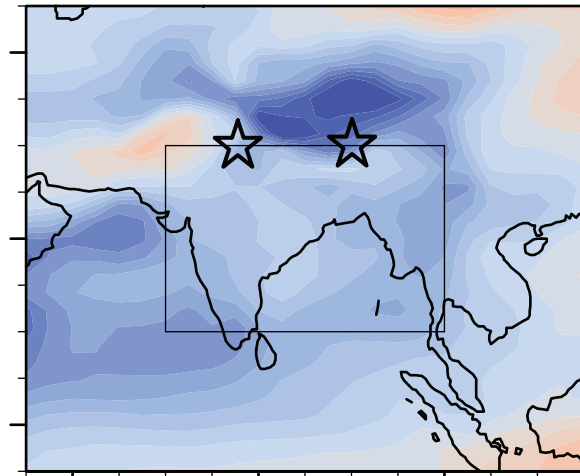


a)Ann $\delta^{18}\text{O}$ precip: WSOL

60E 80E 100E

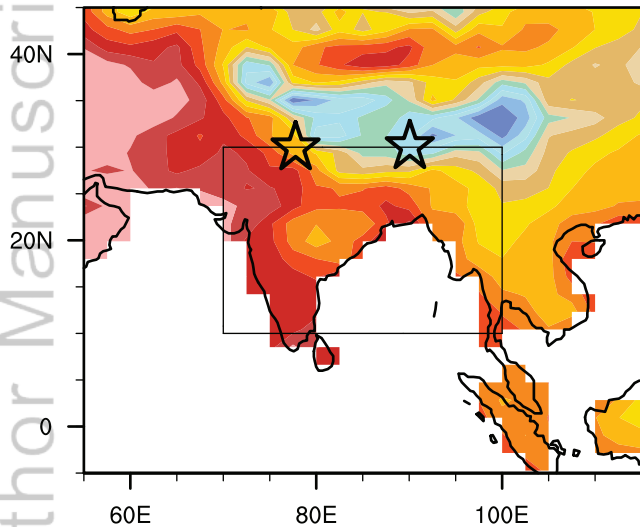
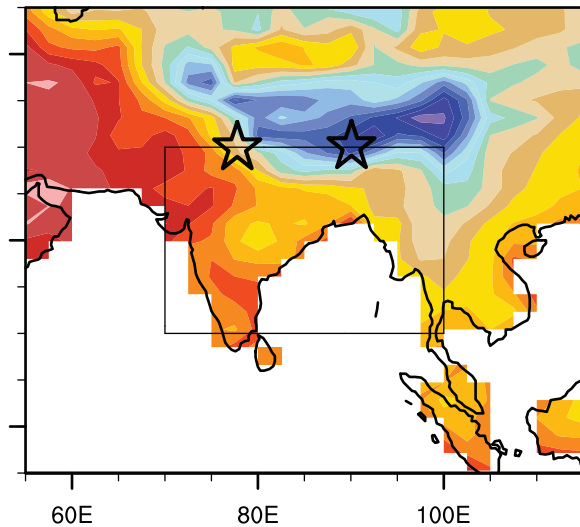
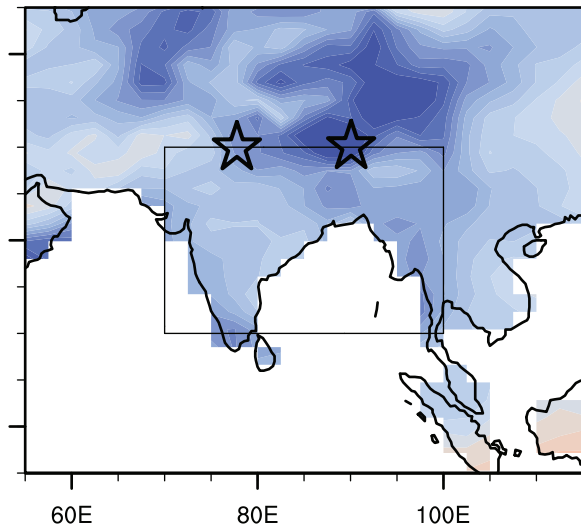
-20 -18 -16 -14 -12 -10 -8 -6 -4
per mil**b)**Ann $\delta^{18}\text{O}$ prec: SSOL

60E 80E 100E

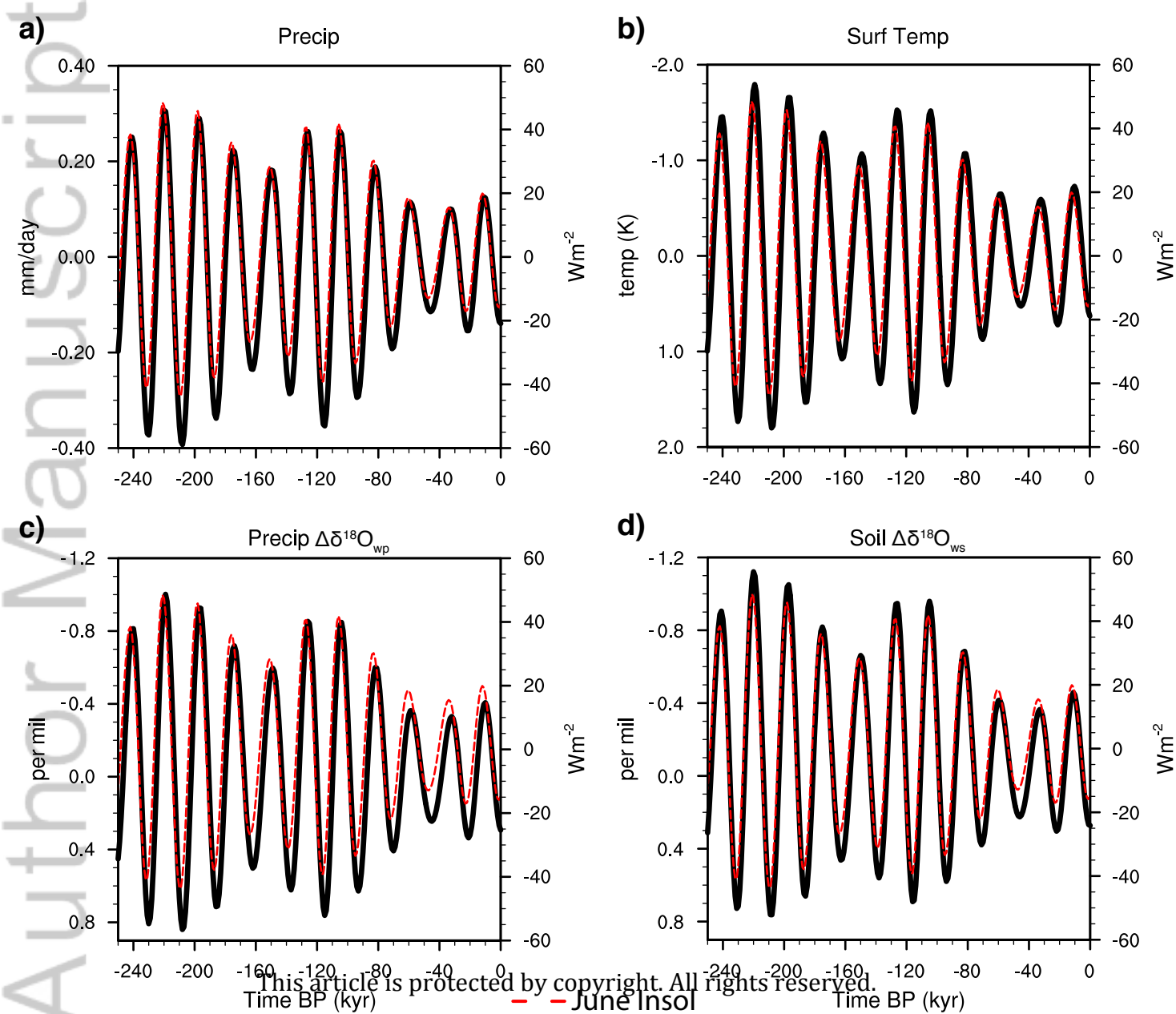
-20 -18 -16 -14 -12 -10 -8 -6 -4
per mil**c)**Ann $\delta^{18}\text{O}$ precip: SSOL - WSOL

60E 80E 100E

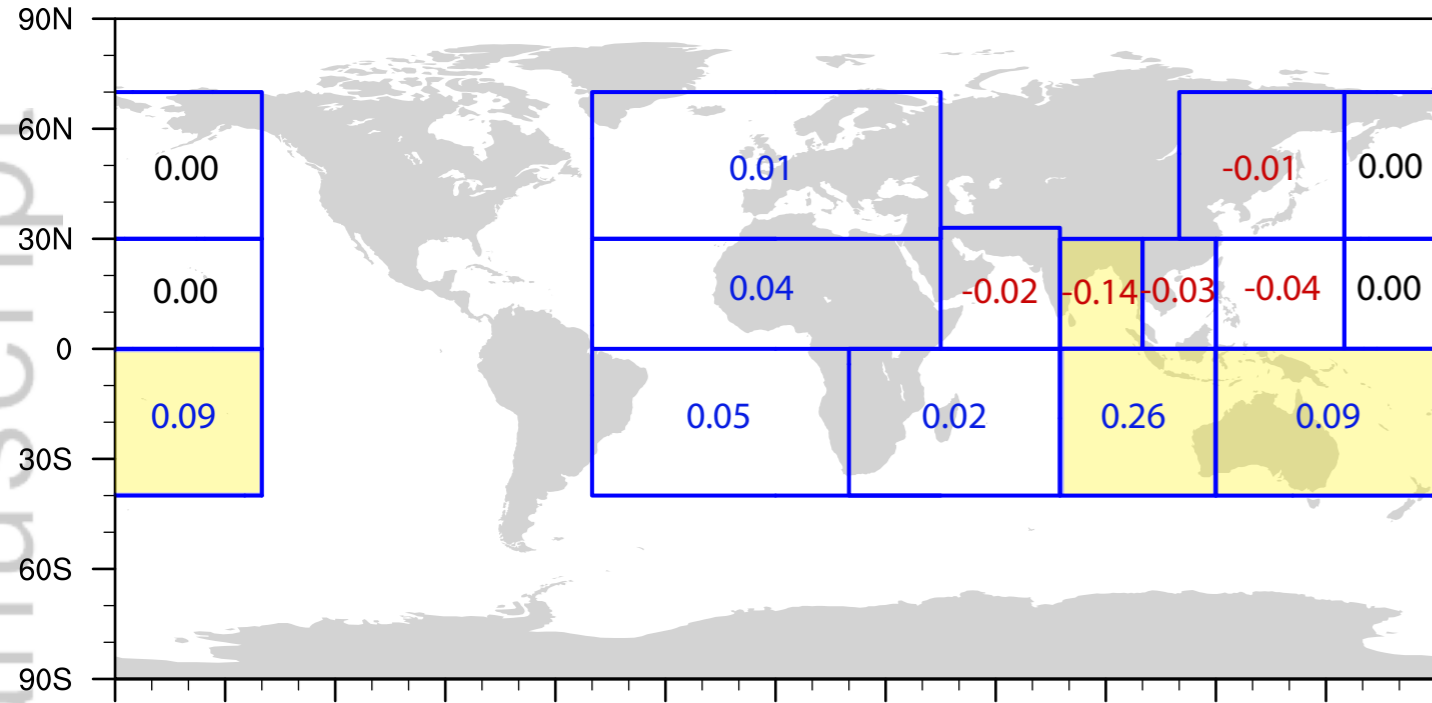
-3.6 -2.4 -1.2 0 1.2 2.4 3.6
per mil

a)Ann 10cm $\delta^{18}\text{O}$ soil: WSOL**b)**Ann 10cm $\delta^{18}\text{O}$ soil: SSOL**c)**Ann 10cm $\delta^{18}\text{O}$ soil: SSOL - WSOL

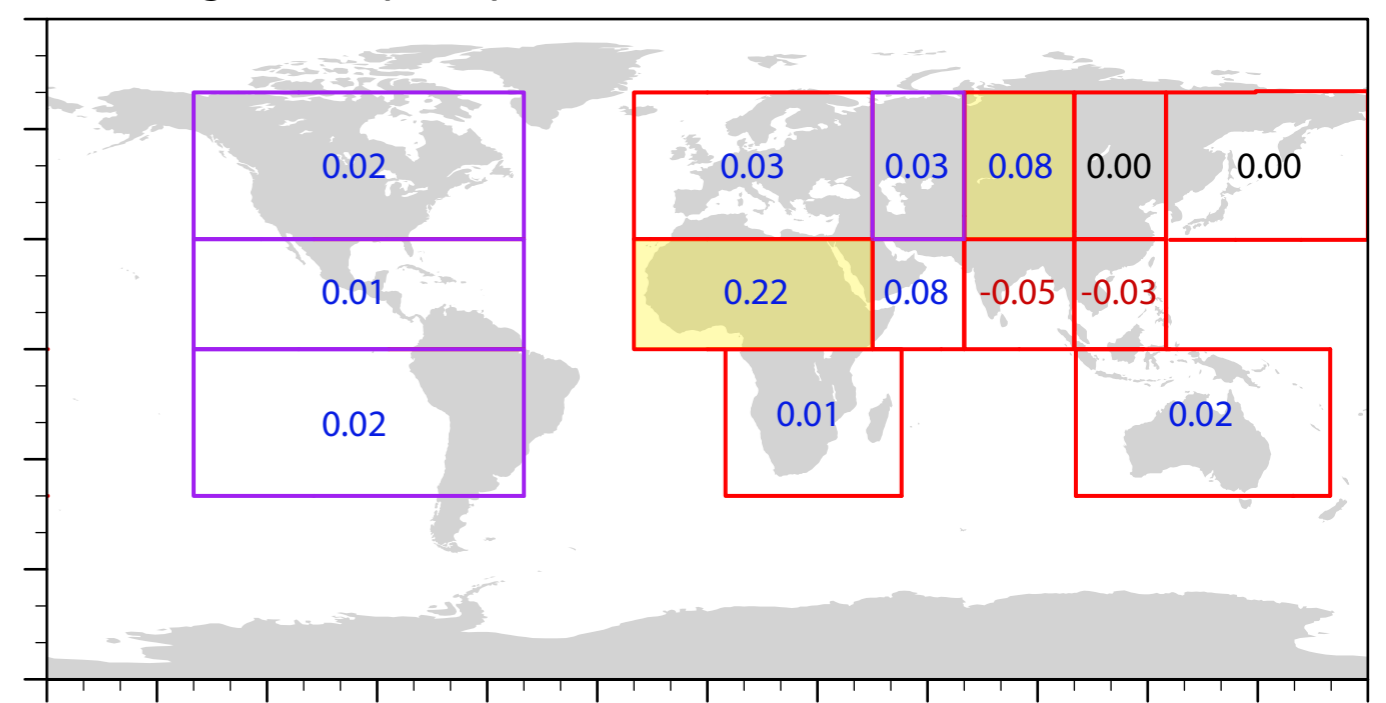
This article is protected by copyright. All rights reserved.



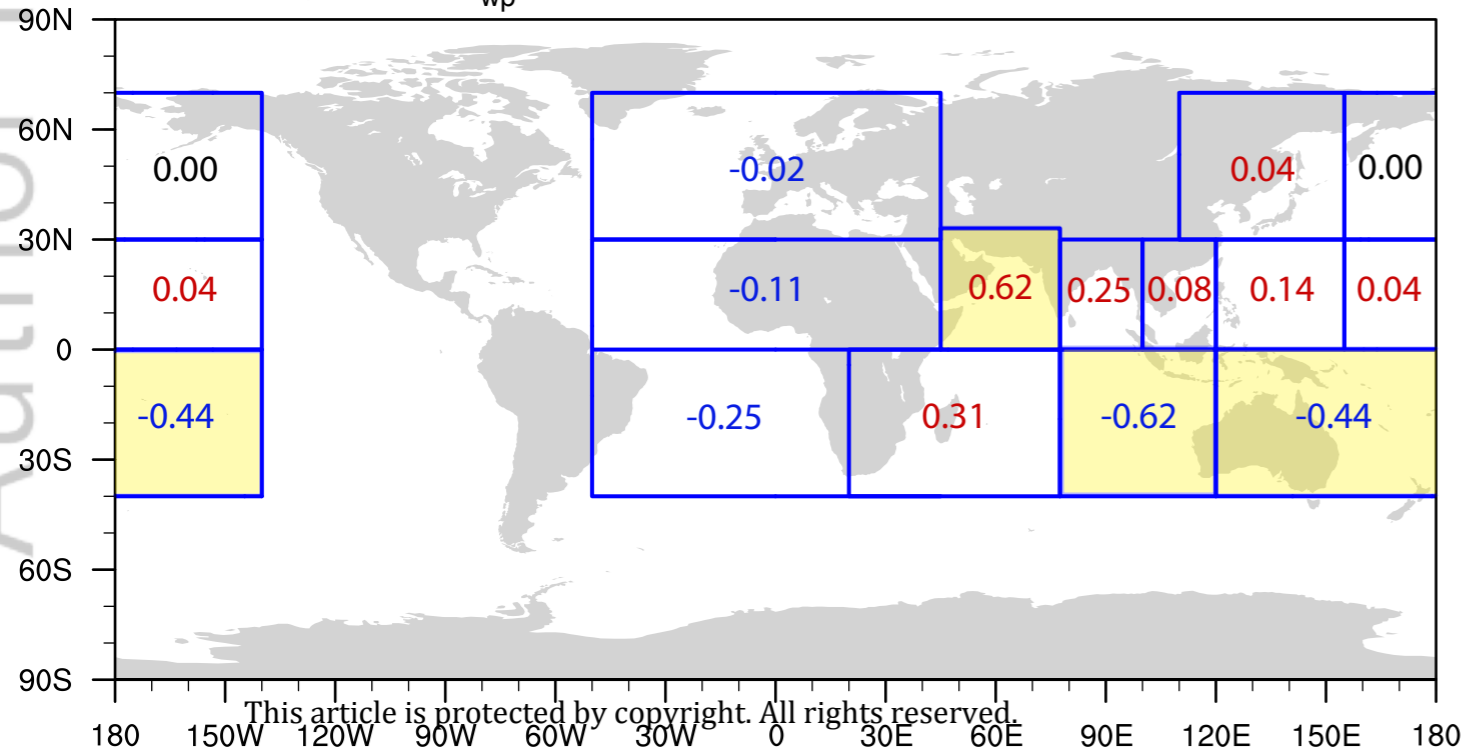
a) Ocean Tags Δ Precip Response: SSOL - WSOL



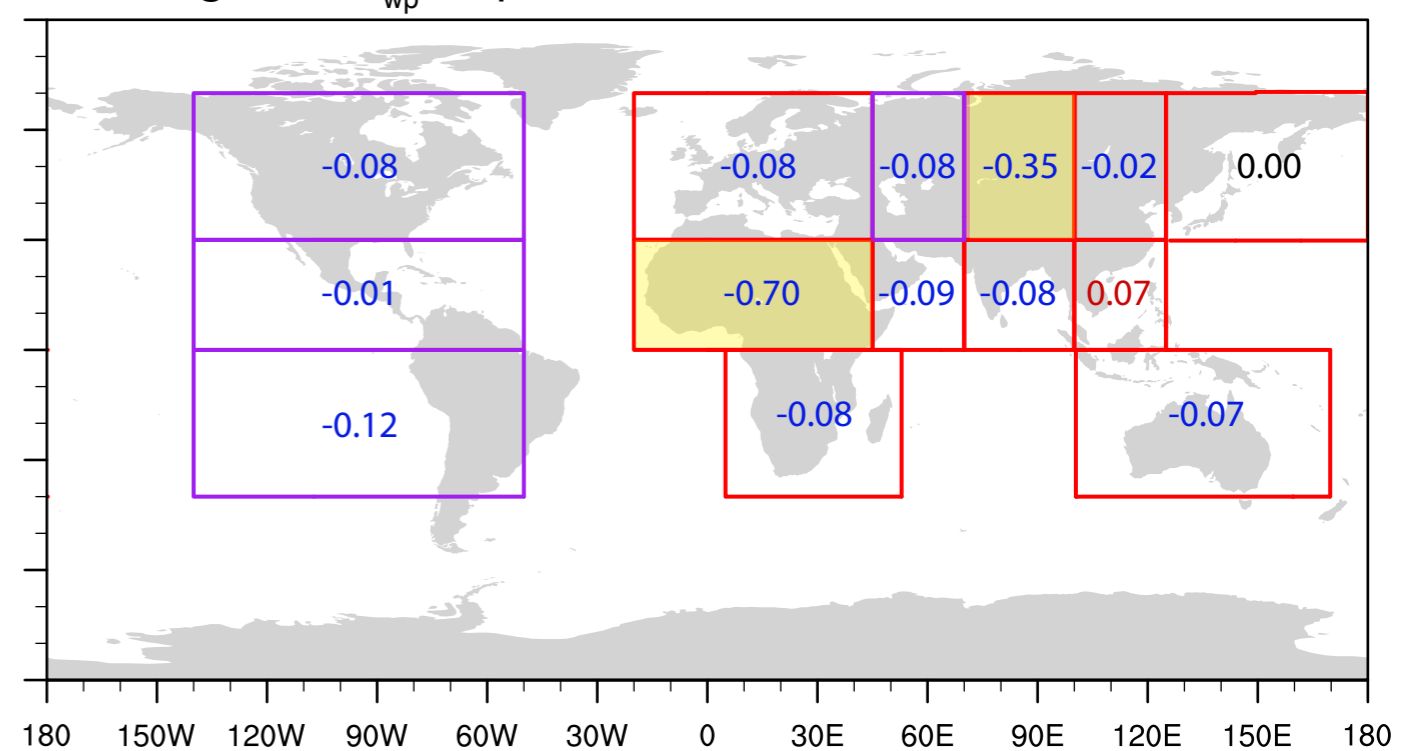
b) Land Tags Δ Precip Response: SSOL - WSOL



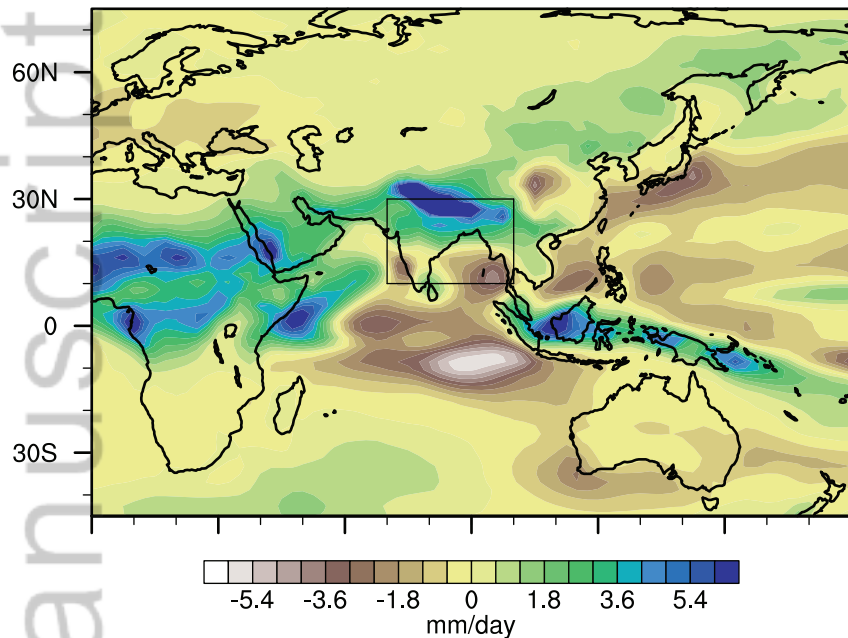
c) Ocean Tags $\Delta\delta^{18}O_{wp}$ Response: SSOL - WSOL



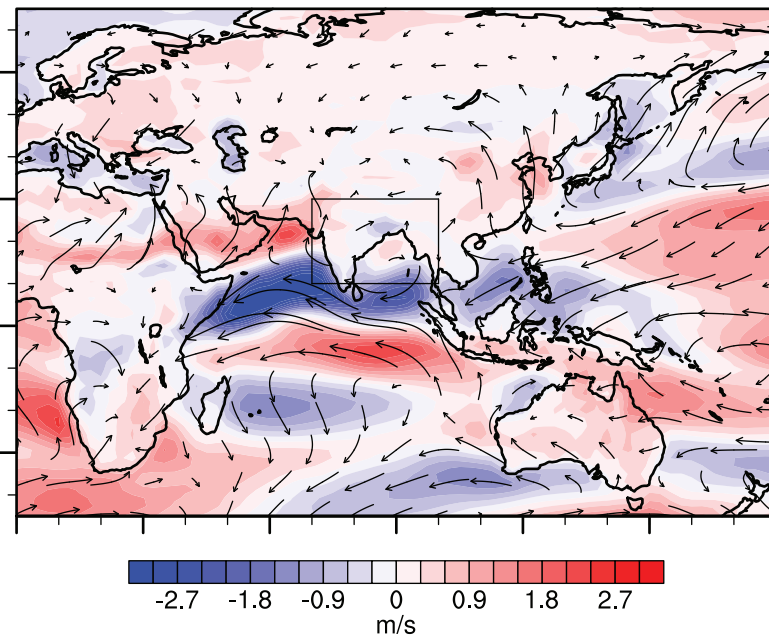
d) Land Tags $\Delta\delta^{18}O_{wp}$ Response: SSOL - WSOL



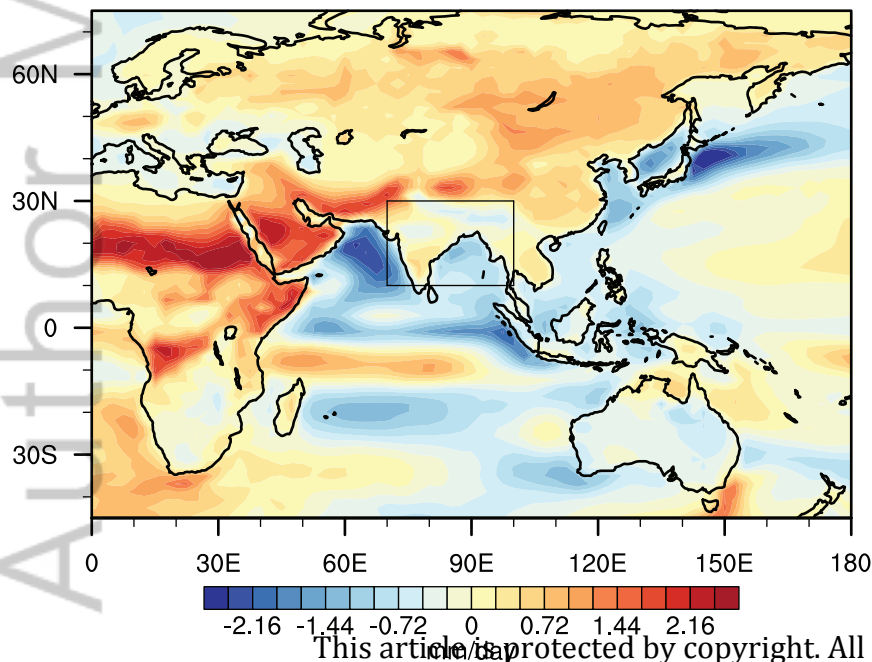
a) JJAS Precip: SSOL - WSOL



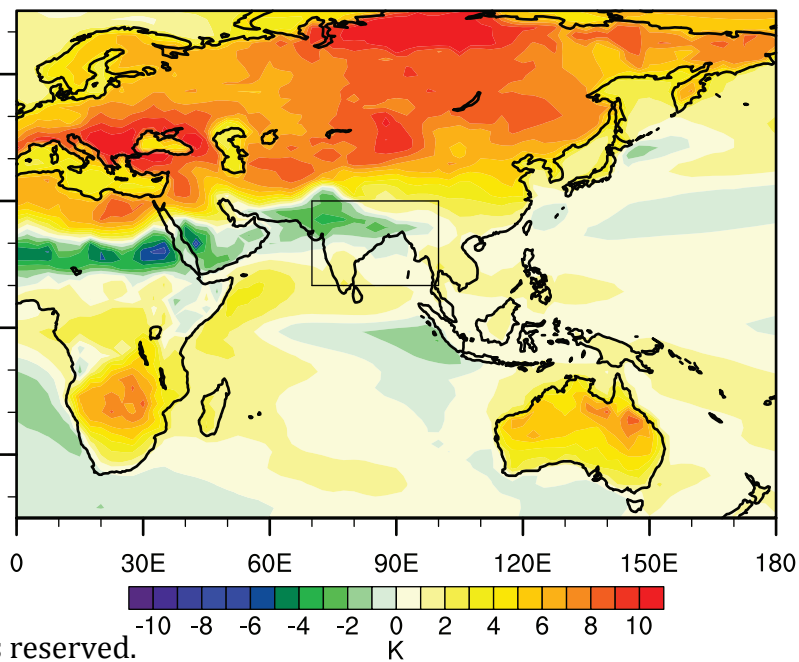
b) JJAS Wind: SSOL - WSOL

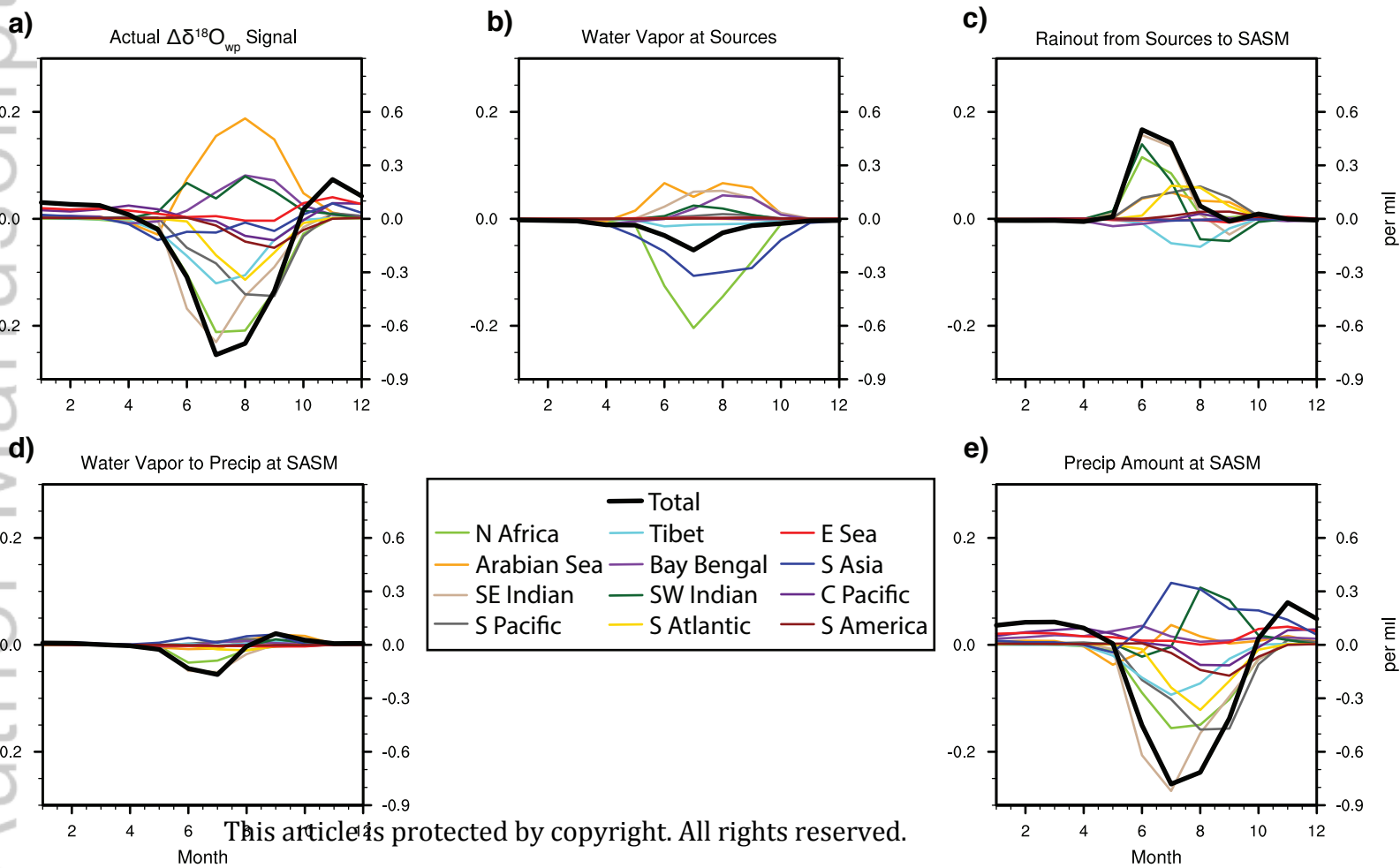


c) JJAS Evap: SSOL - WSOL



d) JJAS Surf Temp: SSOL - WSOL





Amount Effect

